



Atmospheric degradation of dimethyl sulfone mediated by $\bullet\text{OH}$, $\bullet\text{Cl}$ and $\text{NO}_3\bullet$, and the C-centered dimethyl sulfone radical + $^3\text{O}_2$ reaction: A kinetics and mechanistic study

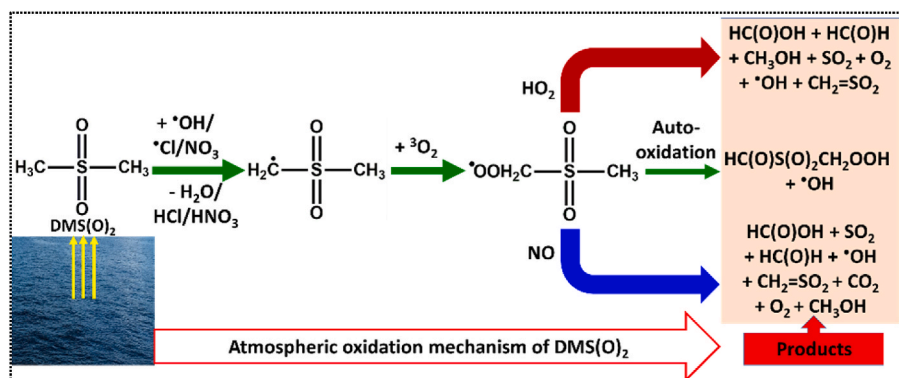
Parandaman Arathala, Rabi A. Musah*

University at Albany—State University of New York, Department of Chemistry, 1400 Washington Avenue, Albany, NY, 12222, USA

HIGHLIGHTS

- Detailed theoretical mechanistic and kinetic study of $\text{CH}_3\text{S}(\text{O})_2\text{CH}_3 + \bullet\text{OH}/\bullet\text{Cl}/\text{NO}_3\bullet$
- Energetics and kinetics report of $\text{CH}_3\text{S}(\text{O})_2\text{CH}_2 + ^3\text{O}_2$ reaction
- Computed rate coefficients agree well with known experimental values.
- $\text{CH}_3\text{S}(\text{O})_2\text{CH}_3$ oxidation results in formation of multiple greenhouse gases.
- $\text{CH}_3\text{S}(\text{O})_2\text{CH}_3$ oxidation products may contribute to global warming.

GRAPHICAL ABSTRACT



ARTICLE INFO

Keywords:

Dimethyl sulfone
OH radical
Cl atom
 NO_3 radical
Rate coefficient
Atmospheric lifetime

ABSTRACT

Mechanistic and kinetics studies of the gas phase reactions of dimethyl sulfone ($\text{DMS}(\text{O})_2$; $\text{CH}_3\text{S}(\text{O})_2\text{CH}_3$) mediated by hydroxyl radical ($\bullet\text{OH}$), chlorine atom ($\bullet\text{Cl}$) and nitrate radical ($\text{NO}_3\bullet$) have been extensively investigated using quantum chemistry calculations along with kinetic modeling. The reaction of $\text{DMS}(\text{O})_2 + \bullet\text{OH}/\bullet\text{Cl}/\text{NO}_3\bullet$ can in principle undergo abstraction and substitution pathways. The results revealed the dominant path to be abstraction of an H-atom from the methyl group of $\text{DMS}(\text{O})_2$ by $\bullet\text{OH}$, $\bullet\text{Cl}$ and $\text{NO}_3\bullet$, with barriers of 2.1, 4.2, and 9.8 kcal mol^{-1} respectively relative to their starting reactants, to produce $\text{CH}_2\text{S}(\text{O})_2\text{CH}_3$. The barrier heights for the substitution paths involved in the $\text{DMS}(\text{O})_2 + \bullet\text{OH}$, $\text{DMS}(\text{O})_2 + \bullet\text{Cl}$ and $\text{DMS}(\text{O})_2 + \text{NO}_3\bullet$ reactions were found to be very high ($>30 \text{ kcal mol}^{-1}$) and therefore inaccessible under tropospheric conditions. The rate coefficients for all possible H-atom abstractions associated with the $\text{DMS}(\text{O})_2 + \bullet\text{OH}$, $\text{DMS}(\text{O})_2 + \bullet\text{Cl}$ and $\text{DMS}(\text{O})_2 + \text{NO}_3\bullet$ reactions were calculated using Master equation solver for multi-energy well reactions (MESMER) code in the temperature range of 200–320 K and 1 atm. The overall rate coefficients for the reaction of $\text{DMS}(\text{O})_2$ initiated by OH radical, Cl atom and NO_3 radical at 298 K and 1 atm were estimated to be 4.6×10^{-13} , 9.1×10^{-14} and $3.7 \times 10^{-15} \text{ cm}^3 \text{ molecule}^{-1} \text{ s}^{-1}$, respectively. The atmospheric lifetime of $\text{DMS}(\text{O})_2$ with respect to its reactions with $\bullet\text{OH}$, $\bullet\text{Cl}$ and $\text{NO}_3\bullet$ was also estimated. The major product $\text{CH}_2\text{S}(\text{O})_2\text{CH}_3$ further reacts with ground state molecular oxygen ($^3\text{O}_2$) to form the $\text{CH}_3\text{S}(\text{O})_2\text{CH}_2\text{OO}\bullet$ adduct. Computational methods also showed that the rate

* Corresponding author.

E-mail address: rmusah@albany.edu (R.A. Musah).

<https://doi.org/10.1016/j.atmosenv.2023.119990>

Received 1 June 2023; Received in revised form 17 July 2023; Accepted 30 July 2023

Available online 1 August 2023

1352-2310/© 2023 Elsevier Ltd. All rights reserved.

of unimolecular isomerization of the $\text{CH}_3\text{S}(\text{O})_2\text{CH}_2\text{OO}^\bullet$ adduct is slow compared to its reactions with NO and hydroperoxyl (HO_2) radical. Ultimately, the $\text{CH}_3\text{S}(\text{O})_2\text{CH}_2\text{OO}^\bullet$ adduct leads to formation of formic acid, sulfur dioxide, formaldehyde, methanol, carbon dioxide, sulfene, and OH radical as final products under high NO and HO_2 radical atmospheric conditions.

1. Introduction

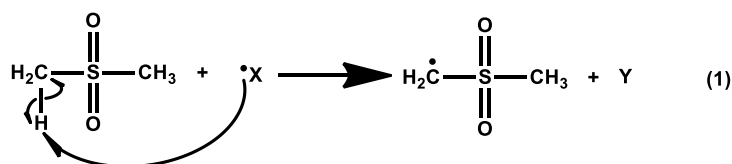
The oceans represent an important source of volatile organosulfur compounds (VOSCs) and strongly influence the global sulfur cycle (Bentley and Chasteen, 2004; Brimblecombe, 2013; Sievert et al., 2007). Dimethyl sulfide (DMS; CH_3SCH_3) is a biogenic source of sulfur, mainly produced by phytoplankton. The global DMS flux in the atmosphere is estimated to be 28.1 Tg S per year, about 50% of which is attributed to anthropogenic contributions (Edtbauer et al., 2020; Webb et al., 2019). Thus, DMS is an important contributor to the global sulfur budget. The fate of DMS and its transformation mechanisms are very complex and still not fully understood (Ayers and Gillett, 2000; Barnes et al., 2006; Chen et al., 2018; Mardyukov and Schreiner, 2018). The reaction of DMS with OH radical is considered to be the dominant loss process (Khan et al., 2016). Several studies indicate that the tropospheric oxidation of DMS produces sulfur dioxide (SO_2), sulfuric acid (H_2SO_4), methanesulfonic acid and dimethyl sulfoxide (DMSO) as products (Cox et al., 1997; Jensen et al., 1991; Tyndall and Ravishankara, 1991; Yin et al., 1990). Some studies indicate that dimethyl sulfone ($\text{DMS}(\text{O})_2$; $\text{CH}_3\text{S}(\text{O})_2\text{CH}_3$) is an important product formed from the oxidation of DMS with OH radical (Arsene et al., 2001; Barnes et al., 2006). It is also reported that $\text{DMS}(\text{O})_2$ is produced from the oxidation of DMSO with BrO and NO_3 radicals (Barnes et al., 2006). This compound has been detected in gas phase and rainwater samples (Berresheim et al., 1993; Davis et al., 1998; Harvey and Lang, 1986; Watts et al., 1990). In a recent study, the concentration of $\text{DMS}(\text{O})_2$ in the Arabian Sea region was found to range between 40 and 120 parts per trillion (ppt) (Edtbauer et al., 2020). This suggests that $\text{DMS}(\text{O})_2$ is a ubiquitous molecule in the atmosphere. However, its fate under tropospheric conditions is not fully understood.

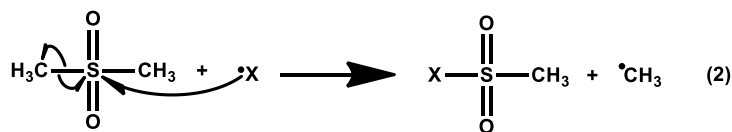
Because the major oxidative degradation of volatile organic compounds (VOCs) in the troposphere is known to be their reaction with OH radical (Ball, 2000; Riedel and Lassey, 2008), the reaction of $\text{DMS}(\text{O})_2$ with $^\bullet\text{OH}$ is expected to be a major gas phase removal process in the troposphere. Similar to other VOSCs, atmospheric removal of $\text{DMS}(\text{O})_2$ may proceed by other mechanisms including photolysis, and degradation initiated by $^\bullet\text{OH}$, NO_3^\bullet , and $^\bullet\text{Cl}$. Once released into the atmosphere, $\text{DMS}(\text{O})_2$ may be expected to interact with OH radicals during the daytime. NO_3 radicals are an important species present in nighttime atmospheres. Ozone (O_3) concentrations in the atmosphere range between 5 and 50 parts per billion (ppb) at night. The reaction of $\text{O}_3 + \text{NO}_2$ leads to formation of NO_3 radicals, whose concentrations can reach 1 ppt (Khan et al., 2008; Nøjgaard, 2010). Therefore, atmospheric NO_3 radical can be an important nighttime oxidant in polluted areas with high NO_x levels (Draper et al., 2015; Lee et al., 2016; Rollins et al., 2012). In addition, Cl atoms are another important species present at

concentrations that range from 1 to 10% that of OH radical levels under marine boundary layer (MBL) conditions, as well as in polluted industrial areas (Nicovich et al., 2015; Wingenter et al., 2005). Also, rate coefficients for the reaction of Cl atoms with VOCs are reported to be almost an order of magnitude larger than the corresponding OH radical reactions (Atkinson et al., 1989; Wang et al., 2002; Xie et al., 2015). This suggests that Cl atom reactions are also important at MBLs, and in polluted marine and industrial areas.

Reports of the oxidation of $\text{DMS}(\text{O})_2$ initiated by the $^\bullet\text{OH}$, $^\bullet\text{Cl}$ and NO_3^\bullet under tropospheric conditions are very limited. The kinetics and products of the gas phase oxidation of $\text{DMS}(\text{O})_2$ mediated by $^\bullet\text{OH}$, NO_3^\bullet , and Cl atom have been studied using the relative rate technique (Falbe-Hansen et al., 2000). The rate coefficients for these reactions at 298 K were reported to be $k(\text{DMSO}_2 + ^\bullet\text{OH}) = <3.0 \times 10^{-13}$; $k(\text{DMSO}_2 + \text{NO}_3^\bullet) = <2.0 \times 10^{-15}$; and $k(\text{DMSO}_2 + ^\bullet\text{Cl}) = (2.4 \pm 0.8) \times 10^{-14} \text{ cm}^3 \text{ molecule}^{-1} \text{ s}^{-1}$ (Falbe-Hansen et al., 2000). To date, no studies investigating the mechanism and kinetics of the gas phase oxidation of $\text{DMS}(\text{O})_2$ mediated by $^\bullet\text{OH}$, $^\bullet\text{Cl}$ and NO_3^\bullet under tropospheric conditions have appeared. Therefore, to investigate the transformation process of $\text{DMS}(\text{O})_2$ in the troposphere, we performed high level ab initio/DFT electronic structure calculations on its reactions with these major atmospheric oxidants. In addition, since the experimentally measured rate coefficients for these reactions were reported at 298 K only, we computed the rate coefficients for these reactions in the atmospherically relevant temperature range between 200 and 320 K. This range was selected because while the reactions have been explored experimentally using the relative rate technique at 298 K, kinetics information about the reaction over the full range of atmospherically relevant temperatures, which is essential in order to accomplish atmospheric modeling, remains unknown. Thus, it was anticipated that this study would provide important information about the atmospheric chemistry of $\text{DMS}(\text{O})_2$ in the presence of $^\bullet\text{OH}$, $^\bullet\text{Cl}$ and NO_3^\bullet . Using the rate coefficient results, we estimated the atmospheric lifetime of $\text{DMS}(\text{O})_2$ in the studied temperature range. From the results, we propose a transformation mechanism for the degradation of $\text{DMS}(\text{O})_2$ in the atmosphere.

The oxidation of $\text{DMS}(\text{O})_2$ in the presence of OH radical, Cl atom and NO_3 radical can in principle undergo H-atom abstraction and substitution pathways (see eqns. 1 and 2). The abstraction of an H-atom from the methyl group of $\text{DMS}(\text{O})_2$ by any atmospheric oxidant (X) to form products (C-atom centered $\text{DMS}(\text{O})_2$ radical + Y) is shown in eqn. 1. On the other hand, the substitution path would proceed by addition of X to the S-atom of the $-\text{S}(\text{O})_2$ group, followed by $\text{H}_3\text{C}-\text{S}(\text{O})_2$ single bond rupture leading to formation of products ($^\bullet\text{CH}_3 + \text{CH}_3\text{S}(\text{O})_2\text{X}$) as shown in eqn. 2. In eqns. 1 and 2, X can be OH radical, Cl atom or NO_3 radical, and Y can be H_2O , HCl or HNO_3 , respectively.





We investigated the reactions illustrated in eqns. 1 and 2 by characterizing the corresponding intermediate pre-reactive and product complexes (PRCs and PCs), transition states (TSs), and products on the potential energy surface (PES) profiles using a combination of *ab initio*/DFT electronic structure calculations along with kinetic modeling. The results of this work provide greater insight into the atmospheric chemistry of $\text{DMS}(\text{O})_2$ under tropospheric conditions.

2. Computational details

We used quantum chemical calculations to better understand the degradation mechanism of $\text{DMS}(\text{O})_2$ mediated by $\cdot\text{OH}$, $\cdot\text{Cl}$ and $\text{NO}_3\cdot$. The calculations were performed by following three major steps. In the first step, the M06-2X hybrid density functional (Zhao and Truhlar, 2008) along with the aug-cc-pV(T+d)Z basis set (Jr. et al., 2001) was used for geometry optimization of all the key stationary points on the PESs associated with the reactions of $\text{DMS}(\text{O})_2 + \cdot\text{OH}$, $\text{DMS}(\text{O})_2 + \cdot\text{Cl}$ and $\text{DMS}(\text{O})_2 + \text{NO}_3\cdot$. Reaction mechanisms, hydrogen bonding interactions, and calculation of the energetics and kinetics have been successfully computed using this level of theory for various important atmospheric reactions (Arathala and Musah, 2022, 2023; Chen et al., 2021; Xie et al., 2015). Various studies of oxidation reactions of several atmospheric molecules initiated by $\cdot\text{Cl}$ and $\text{NO}_3\cdot$, have used the M06-2X method for geometry optimization (Anglada and Solé, 2017; Arathala and Musah, 2021; Lily et al., 2020; Maguta et al., 2016; Rao et al., 2018). All of these reports indicate that this level of theory provides accurate structures and energies that reveal the nature of these reactions under atmospheric conditions. In addition, an extra set of tight *d*-functions were added in the aug-cc-pV(T+d)Z basis set in order to better simulate bonding in the S-containing compounds (Kurtén et al., 2011; Wilson and Dunning, 2004). Harmonic vibrational frequency calculations were performed at the same level of theory to verify that all the stationary points on the PESs represented local minima or transition states. To optimize all the transition states, we used the command OPT = TS developed in the Gaussian 16 program (Frisch et al., 2016). In the second step, Intrinsic Reaction Coordinate (IRC) calculations were performed at the same M06-2X/aug-cc-pV(T+d)Z level for each of the TSs obtained in this work to determine whether they were connected with their respective PRCs and PCs (Fukui, 1981). In the third step, we performed CCSD(T)/aug-cc-pV(T+d)Z level single point energy calculations on all the stationary points optimized at the M06-2X/aug-cc-pV(T+d)Z level to refine the energies for all the possible paths (Noga and Bartlett, 1987). Finally, single point energies for all the stationary points obtained at the CCSD(T)/aug-cc-pV(T+d)Z level were corrected with zero-point energies (ZPE) obtained at the M06-2X/aug-cc-pV(T+d)Z level (defined as CCSD(T)//M06-2X). The computed electronic energies and ZPE's for all of the stationary points associated with the reactions of $\text{DMS}(\text{O})_2 + \cdot\text{OH}$, $\text{DMS}(\text{O})_2 + \cdot\text{Cl}$ and $\text{DMS}(\text{O})_2 + \text{NO}_3\cdot$ obtained at various levels are displayed in Table S1.

3. Results and discussion

3.1. Electronic structure calculations and energetics

The C-atoms of both methyl groups of $\text{DMS}(\text{O})_2$ are attached to the S-atom of the $-\text{S}(\text{O})_2$ moiety. However, due to the spatial orientations of the methyl group hydrogens with respect to the $-\text{S}(\text{O})_2$ group, not all the

hydrogen atoms that are attached to the same carbon are equivalent. For a given methyl group, the two hydrogens that are oriented away from the O-atoms of the $\text{S}(\text{O})_2$ group are equivalent, while the third hydrogen which is oriented towards the O-atoms of $\text{S}(\text{O})_2$ represent a second type of hydrogen. Thus, H-abstraction (eqn. 1) can take place by more than one pathway. The transition state labelled TS1 corresponds to OH radical abstraction of either of the two hydrogens that are oriented away from the O-atoms of the $\text{S}(\text{O})_2$ group. TS2 corresponds to abstraction by OH radical of the H-atom that is oriented towards the O-atoms of the $\text{S}(\text{O})_2$ group. The substitution pathway (eqn. 2) involved in the $\text{DMS}(\text{O})_2 + \text{OH}$ radical reaction is associated with TS3. Similarly, the transition states for the H-abstraction and substitution paths associated with the $\text{DMS}(\text{O})_2 + \text{Cl}$ atom reaction are labelled TS4, TS5, and TS6; and the transition states associated with the H-abstraction and substitution paths for the $\text{DMS}(\text{O})_2 + \text{NO}_3\cdot$ radical reaction are labelled TS7, TS8, and TS9, respectively.

Optimized geometries of the reactants, PRCs, TSs, PCs and products for the hydrogen atom abstraction and substitution paths involved in the reaction of $\text{DMS}(\text{O})_2 + \cdot\text{OH}$, $\text{DMS}(\text{O})_2 + \cdot\text{Cl}$ and $\text{DMS}(\text{O})_2 + \text{NO}_3\cdot$ are shown in Fig. 1, Fig. S1 and Fig. S2, respectively. Important bond lengths computed at the M06-2X/aug-cc-pV(T+d)Z level are provided in the structures of these figures. The harmonic vibrational frequencies, rotational constants for all the stationary points, imaginary frequencies of the various TSs and the optimized geometries of all of the stationary points involved in the title reactions are displayed in Tables S2–S5.

The zero-point corrected CCSD(T)//M06-2X level calculated PES profiles involving all of the key stationary points for the possible H-abstraction and substitution paths associated with the reaction of $\text{DMS}(\text{O})_2 + \cdot\text{OH}$; $\text{DMS}(\text{O})_2 + \cdot\text{Cl}$; and $\text{DMS}(\text{O})_2 + \text{NO}_3\cdot$ are shown in Figs. 2a, 3a and 4a. The energies of all the minima and transition states displayed in the figures were estimated relative to the energies of the corresponding separated reactants at the ZPE corrected CCSD(T)//M06-2X level. The data from Figs. 2a, 3a and 4a suggest that the interaction of any atmospheric oxidant such as OH radical, Cl atom or $\text{NO}_3\cdot$ radical with the $\text{DMS}(\text{O})_2$ molecule initially forms stable PRCs through hydrogen bonding. This can be clearly seen at each entrance channel of their reaction PESs (see Figs. 2a, 3a and 4a). In the next step, the PRCs proceed to form their respective PCs through their corresponding TSs. Finally, the PCs undergo unimolecular decomposition to form final products (see the exit channels in Figs. 2a, 3a and 4a).

3.1.1. $\text{DMS}(\text{O})_2 + \text{OH}$ radical

We found two different hydrogen bonded complexes (PRC1 and PRC2) between the $\text{DMS}(\text{O})_2$ molecule and OH radical (see Figs. 1 and 2a), with respective binding energies of -5.7 and $-5.1 \text{ kcal mol}^{-1}$. PRC1 and PRC2 have cyclic structures with three intramolecular hydrogen bonds. The structure of PRC1 indicates a strong hydrogen bond between a hydrogen atom of OH and one of the O-atoms of the $\text{S}(\text{O})_2$ group with a bond length of 1.95 Å , and two other weak hydrogen bonds between the H-atoms of the two methyl groups and the O-atom of the OH radical (with corresponding bond distances computed to be 2.42 and 2.63 Å —see Fig. 1). In PRC2, a strong H-bond between the H-atom of OH and one of the O-atoms of the $\text{S}(\text{O})_2$ group (with a bond distance found to be 1.93 Å), and two other weak H-bonds between the O-atom of OH and the other two H-atoms of the same methyl group (with their respective computed bond lengths of 2.49 and 2.76 Å) were observed. PRC1 was found to be the most stable with a binding energy of $-5.7 \text{ kcal mol}^{-1}$. The zero-point corrected CCSD(T)//M06-2X level calculations indicated

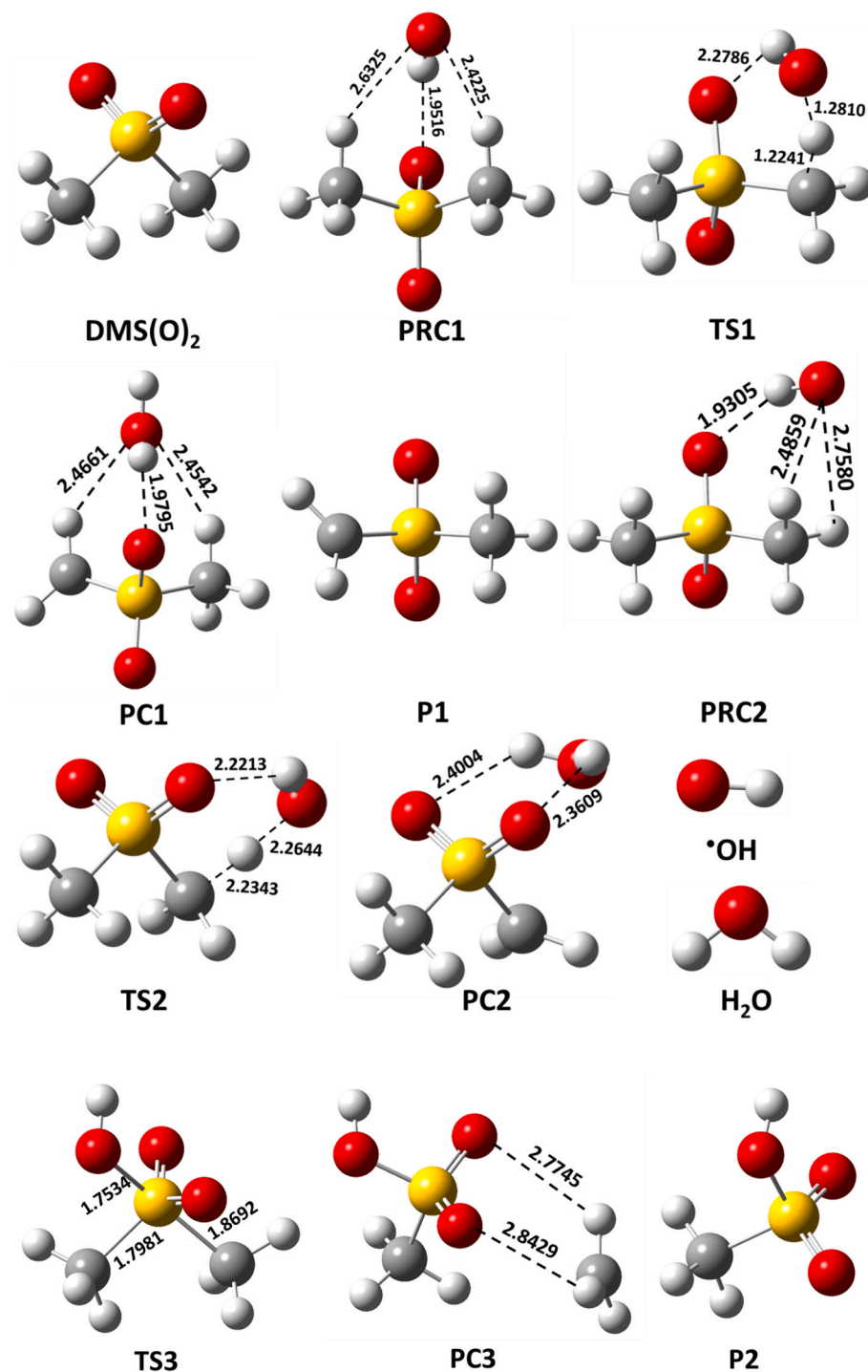
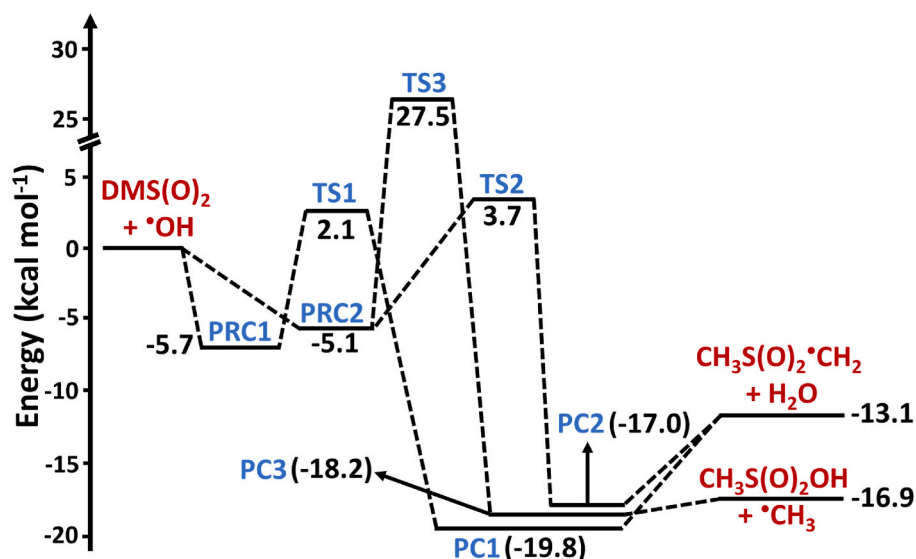


Fig. 1. Optimized geometries of the pre-reactive complexes (PRCs), transition states (TSs), product complexes (PCs), and products (Ps) for the H-abstraction and substitution paths involved in the reaction of dimethyl sulfone + OH radical obtained at the M06-2X/aug-cc-pV(T+d)Z level. The bond lengths (in Å) shown on the structures were computed at the M06-2X/aug-cc-pV(T+d)Z level. The C, S, H, and O-atoms are shown respectively with black, yellow, white, and red colors.

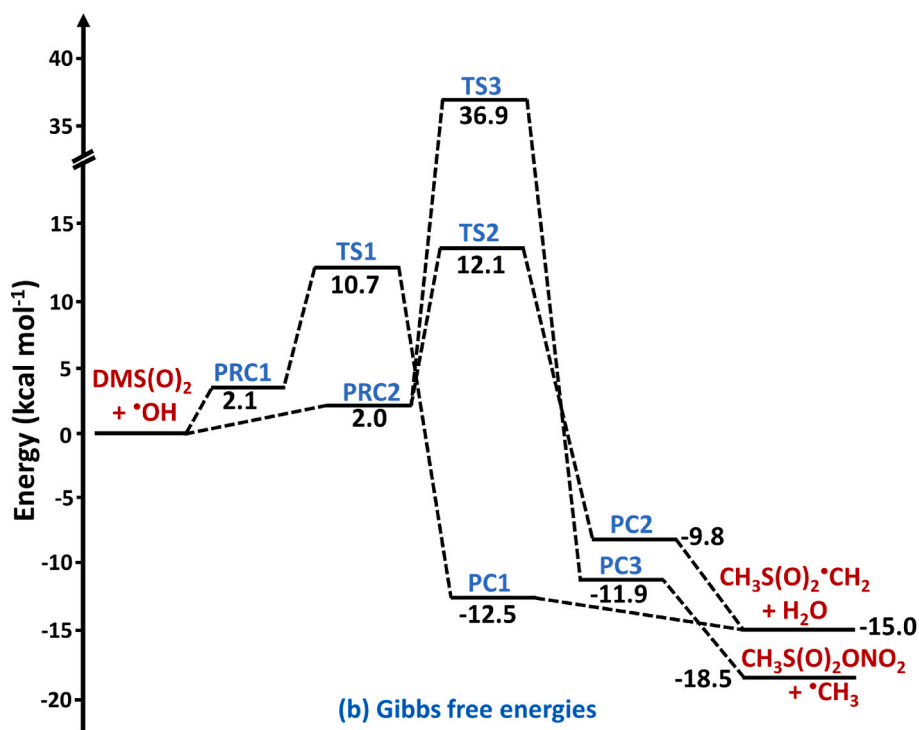
that the energy difference between PRC1 and PRC2 was ~ 0.6 kcal mol⁻¹. Similar to the structure of PRC2, we also noted that an analogous pre-reactive complex was reported in the reaction of methane sulfonamide with OH radical (Arathala and Musah, 2022). The binding energy for this complex was reported to be -5.0 kcal mol⁻¹ using the same computational methods (Arathala and Musah, 2022). This suggests that the binding energy of PRC2 agrees well with the values for the PRC reported for the methane sulfonamide + OH radical reaction (Arathala and Musah, 2022).

Three transition states (TS1, TS2 and TS3) were found for the H-atom

abstraction and substitution paths involved in the DMS(O)_2 + OH radical reaction (see Fig. 2a). TS1 and TS2 are formed from the corresponding PRC1 and PRC2 complexes with barrier heights of 2.1 and 3.7 kcal mol⁻¹ above the starting reactants, respectively. The structures of TS1 and TS2 clearly indicate that abstraction of an H-atom from the methyl group by OH radical occurs in a hydrogen bonded six-membered ring like configuration. The results show that the barrier height of TS1 is ~ 1.6 kcal mol⁻¹ lower than that of TS2. This suggests that H-abstraction from the methyl group of DMS(O)_2 that proceeds via TS1 is the dominant reaction compared to the other possible path. We noted that the same



(a) ZPE-corrected relative energies



(b) Gibbs free energies

Fig. 2. The CCSD(T)/aug-cc-pV(T+d)Z//M06-2X/aug-cc-pV(T+d)Z level calculated: (a) ZPE-corrected relative energies; and (b) Gibbs free energy profiles for the abstraction and substitution paths involving the DMS(O)₂ + OH radical reaction to form their respective products. The symbols PRC1 and PRC2; TS1, TS2, and TS3; and PC1, PC2, and PC3; refer to pre-reactive complexes; transition states; and post-reactive complexes respectively.

complex (PRC2) proceeds to form TS3 for the substitution path involved in the DMS(O)₂ + OH radical reaction. The structure of TS3 suggests that the O-atom of the OH radical attacks the S-atom of S(O)₂, which is followed by S—CH₃ single bond cleavage. The barrier height for formation of TS3 was computed to be 27.5 kcal mol⁻¹ above that of the starting reactants. Based on the computed barriers heights, the formation of TS3 is less favorable due to its high barrier when compared to the possible H-abstraction paths. Therefore, TS1 formation was determined to have a lower barrier and to be more dominant when compared to the other possible H-atom abstraction and substitution paths.

Product complexes (PC1, PC2 and PC3) formed from their respective

transition states were identified on the PES profiles at -19.8, -17.0 and -18.2 kcal mol⁻¹ relative to the energy of the starting DMS(O)₂ + OH radical reactants (see Fig. 2a). PC1 is stabilized by two hydrogen bonds between the H-atoms of the -CH₂ and -CH₃ moieties and the O-atom of molecular water, with corresponding bond lengths of 2.47 and 2.45 Å, and a strong H-bond between an H-atom of water and one of the O-atoms of the S(O)₂, with a bond distance computed to be 1.98 Å (see Fig. 1). The complex PC2 is stabilized by two H-bonds between the O-atoms of S(O)₂ and the H-atoms of water with corresponding bond distances of 2.40 and 2.36 Å (see Fig. 1). Finally, these two complexes undergo unimolecular dissociation to form the same bimolecular products (i.e.,

$\cdot\text{CH}_2\text{S}(\text{O})_2\text{CH}_3 + \text{H}_2\text{O}$). Similarly, PC3 is stabilized by interactions between the two oxygen atoms of the $\text{S}(\text{O})_2$ moiety and the two H-atoms of the methyl group, with bond lengths of 2.77 and 2.84 Å respectively (see Fig. 1). This then proceeds to form products ($\text{CH}_3\text{S}(\text{O})_2\text{OH} + \cdot\text{CH}_3$) with an energy of $-16.9 \text{ kcal mol}^{-1}$ relative to the energy of the starting reactants. The PES profiles of the $\text{DMS}(\text{O})_2 + \text{OH}$ radical reaction suggest that formation of TS3 (substitution path) is less favorable due to its very high barrier compared to the barrier height values of the H-abstraction paths. Therefore, H-abstraction via PRC1, TS1, and PC1 to form $\cdot\text{CH}_2\text{S}(\text{O})_2\text{CH}_3 + \text{H}_2\text{O}$ products was determined to have the lowest barrier and to be the dominant reaction path when compared to the other possible H-atom abstraction and substitution paths.

Fig. 2b shows the Gibbs free energies of all the stationary points for the H-atom abstraction and substitution paths associated with the $\text{DMS}(\text{O})_2 + \cdot\text{OH}$ reaction, calculated at the CCSD(T)/aug-cc-pV(T+d) Z//M06-2X/aug-cc-pV(T+d)Z level. The Gibbs free energy barriers for

all possible paths involved in these reactions were calculated as the Gibbs free energy differences between the corresponding reactants and transition states. The Gibbs free energy barrier values for the $\text{DMS}(\text{O})_2 + \cdot\text{OH}$ reaction via TS1, TS2, and TS3 were found to be 10.7, 12.1, and $36.9 \text{ kcal mol}^{-1}$ respectively (see Fig. 2b). These results imply that H-abstraction from the methyl group through TS1 is the most favorable route.

3.1.2. $\text{DMS}(\text{O})_2 + \text{Cl atom}$

In this case, two pre-reactive complexes (PRC3 and PRC4) were found from association of a $\text{DMS}(\text{O})_2$ molecule and a Cl atom at the entrance channels of the H-abstraction and substitution paths (see Fig. 3a and Fig. S1). The complex PRC3 is stabilized by two weak hydrogen bond interactions between the Cl atom and two of the H-atoms of the methyl group, with corresponding bond distances of 2.84 and 2.82 Å (see Fig. S1). The complex PRC4 is stabilized by a 2-center-3-

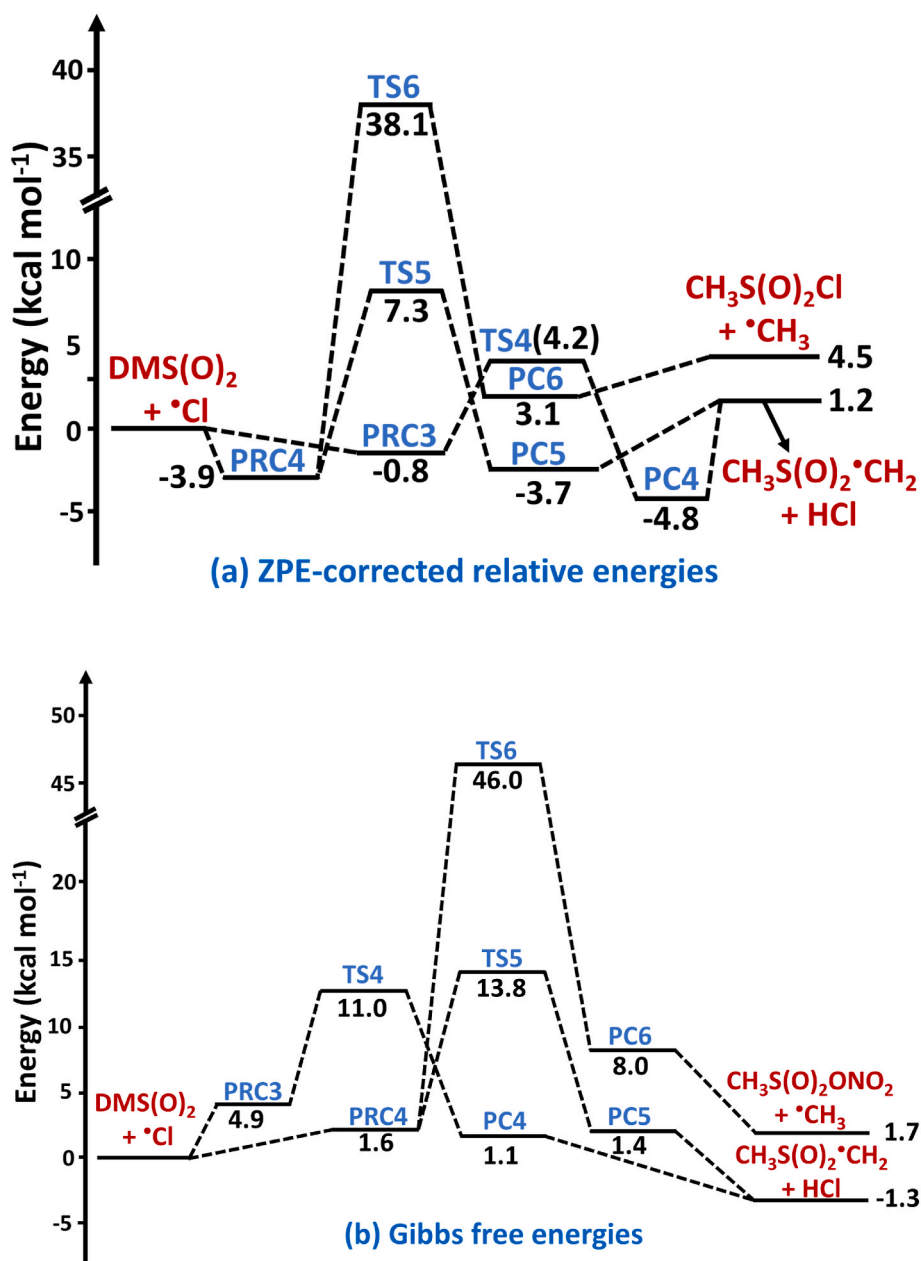


Fig. 3. The CCSD(T)/aug-cc-pV(T+d)Z//M06-2X/aug-cc-pV(T+d)Z level calculated: (a) ZPE-corrected relative energies; and (b) Gibbs free energy profiles for the abstraction and substitution paths associated with the $\text{DMS}(\text{O})_2 + \text{Cl}$ atom reaction to form their respective products. The symbols PRC3 and PRC4; TS4, TS5, and TS6; and PC4, PC5, and PC6; refer to pre-reactive complexes; transition states; and post-reactive complexes respectively.

electron (2c-3e) bond between the lone pair electrons on the O-atom of $\text{DMS}(\text{O})_2$ and a single electron occupied p-orbital of the Cl atom, with a bond length of 2.62 Å. A weak hydrogen bond is also present between an H-atom of the methyl group and the Cl atom, and its bond distance is predicted to be 2.90 Å (see Fig. S1). The binding energies of PRC3 and PRC4 were estimated to be -0.8 and -3.9 kcal mol $^{-1}$ at the CCSD(T)//M06-2X level. Due to the presence of strong van der Waals interactions in PRC4 compared to PRC3, the former complex is ~ 3.0 kcal mol $^{-1}$ more stable than the latter.

These PRCs further lead to the formation of TS4 and TS5 with barrier heights of 4.2 and 7.3 kcal mol $^{-1}$, respectively, above the starting reactants. The structures of TS4 and TS5 show how the Cl atom can abstract an H-atom from the methyl group of $\text{DMS}(\text{O})_2$. TS4 has a lower barrier height (~ 3.0 kcal mol $^{-1}$) compared to the other possible H-abstraction that proceeds via TS5. These TSs further proceed to form PC4 and PC5 at -4.8 and -3.7 kcal mol $^{-1}$ on the PESs. The PC4 structure indicates that the C-atom centered $\text{DMS}(\text{O})_2$ radical and molecular HCl are held together by three H-bonds: one between the H-atom of HCl and one of the O-atoms of $\text{S}(\text{O})_2$; one between an H-atom of the methyl group and the Cl atom of HCl; and one between the H-atom of the methylene group and the Cl atom of HCl; with corresponding bond distances of 1.90, 2.96 and 2.97 Å, respectively. The PC5 structure reveals that the C-atom centered $\text{DMS}(\text{O})_2$ radical and molecular HCl, bind via an H-bond between the H-atom of HCl and one of the O-atoms of the $\text{S}(\text{O})_2$ group, with an H–O bond length computed to be 1.92 Å. Due to the presence of strong H-bonds, complex PC4 was found to be ~ 1.0 kcal mol $^{-1}$ more stable than the complex PC5. PC4 and PC5 further undergo dissociation to form the same pair of products ($^{\bullet}\text{CH}_2\text{S}(\text{O})_2\text{CH}_3 + \text{HCl}$) on the PES at 1.2 kcal mol $^{-1}$. The complex PRC4 also forms a transition state (TS6) for the substitution path involved in the $\text{DMS}(\text{O})_2 + \text{Cl}$ atom reaction, with a barrier height of 38.1 kcal mol $^{-1}$ on the PES. The structure of TS6 suggests Cl atom addition to the S-atom of $\text{S}(\text{O})_2$, followed by cleavage of the S–CH $_3$ bond. The reaction further proceeds to form PC6 which has two hydrogen bonds between the O-atoms of $\text{S}(\text{O})_2$ and the H-atoms of the methyl group, with H–O bond lengths of 2.81 and 2.87 Å. It further leads to products (i.e., $\text{CH}_3\text{S}(\text{O})_2\text{Cl} + ^{\bullet}\text{CH}_3$) at 4.5 kcal mol $^{-1}$ above the starting reactants. The reaction barrier for the substitution channel was found to be 38.1 kcal mol $^{-1}$ which is high compared to the barriers of the H-atom abstraction channels. Therefore, this reaction is energetically less favorable when compared to the H-atom abstraction paths.

Fig. 3b shows the Gibbs free energies of all the stationary points for the H-atom abstraction and substitution paths associated with the $\text{DMS}(\text{O})_2 + ^{\bullet}\text{Cl}$ reaction, calculated at the CCSD(T)/aug-cc-pV(T+d)Z//M06-2X/aug-cc-pV(T+d)Z level. The Gibbs free energy barriers for the $\text{DMS}(\text{O})_2 + ^{\bullet}\text{Cl}$ reactions that proceed via TS4, TS5, and TS6 were found to be 11.0, 13.8, and 46.0 kcal mol $^{-1}$ respectively. These Gibbs free energy barriers reveal that H-abstraction from the methyl group via TS4 is the most dominant path.

3.1.3. $\text{DMS}(\text{O})_2 + \text{NO}_3$ radical

Similar to the results cited above, the association of $\text{DMS}(\text{O})_2$ and NO_3 radical forms two different stable complexes (PRC5 and PRC6) with binding energies of -2.2 and -5.8 kcal mol $^{-1}$, respectively (see Fig. 4a and Fig. S2). PRC5 is stabilized by four hydrogen bonds between the $\text{DMS}(\text{O})_2$ and NO_3 radical, with bond lengths of 2.76, 2.77, 2.80 and 2.80 Å, while PRC6 is stabilized by interactions between: (1) one of the O-atoms of $\text{S}(\text{O})_2$ and the N-atom of the NO_3 radical with an O–N bond distance of 2.76 Å; and a hydrogen bond between an H-atom of the methyl group and one of the O-atoms of the NO_3 radical, with an H–O bond distance predicted to be 2.53 Å (see Fig. S2). The complex PRC6 is more stable by ~ 3.6 kcal mol $^{-1}$ compared to the value for PRC5 (see Fig. 4a). These PRCs proceed further to form TS7 and TS8 with barrier heights of 9.8 and 12.7 kcal mol $^{-1}$ relative to the starting $\text{DMS}(\text{O})_2$ and NO_3 radical reactants. The H-atom abstraction by NO_3 radical from the methyl group of $\text{DMS}(\text{O})_2$ is illustrated in the structures of TS7 and TS8

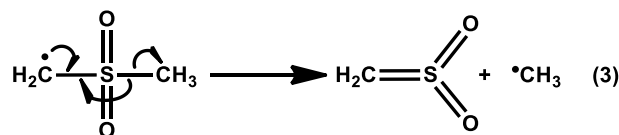
shown in Fig. S2. From Fig. 4a, the barrier height for the formation of TS7 was found to be almost 3.0 kcal mol $^{-1}$ lower than the value of TS8. These H-abstraction paths lead to formation of hydrogen bonded cyclic product complexes (PC7 and PC8) at -13.6 and -11.5 kcal mol $^{-1}$ below the reactants, and then finally to formation of the same pair of products (i.e., $^{\bullet}\text{CH}_2\text{S}(\text{O})_2\text{CH}_3 + \text{HNO}_3$). The substitution path involved in the $\text{DMS}(\text{O})_2 + \text{NO}_3$ radical reaction also starts from PRC6, which then leads to the formation of TS9, with a barrier height of 36.3 kcal mol $^{-1}$ above the reactants. This then connects to PC9 at 0.5 kcal mol $^{-1}$ and then to generation of $\text{CH}_3\text{S}(\text{O})_2\text{ONO}_2 + ^{\bullet}\text{CH}_3$ products. The results suggest that this reaction path has a high barrier compared to the other possible H-abstraction paths. Therefore, abstraction of an H-atom from the methyl group via PRC5, TS7, and PC7 to form $^{\bullet}\text{CH}_2\text{S}(\text{O})_2\text{CH}_3 + \text{HNO}_3$ products was found to have a lower barrier (and therefore be the more dominant reaction) compared to other possible abstraction and substitution paths.

Fig. 4b shows the Gibbs free energies of all the stationary points for the H-atom abstraction and substitution paths associated with the $\text{DMS}(\text{O})_2 + \text{NO}_3^{\bullet}$ reaction, calculated at the CCSD(T)/aug-cc-pV(T+d)Z//M06-2X/aug-cc-pV(T+d)Z level. The calculated Gibbs free energy barriers for the $\text{DMS}(\text{O})_2 + \text{NO}_3^{\bullet}$ reaction via TS7, TS8, and TS9 were estimated to be 20.4, 22.7, and 48.5 kcal mol $^{-1}$ respectively (see Fig. 4b). These results suggest the H-abstraction from the methyl group via TS7 is the most favorable compared to other paths.

Based on the PESs shown in Figs. 2–4, we concluded that the barrier heights and Gibbs free energy barriers for the substitution paths associated with the $\text{DMS}(\text{O})_2 + ^{\bullet}\text{OH}$, $\text{DMS}(\text{O})_2 + \text{Cl}$ atom, and $\text{DMS}(\text{O})_2 + \text{NO}_3$ radical are too high to be accessible under tropospheric conditions. Therefore, these reaction paths were not considered for further kinetic calculations.

3.2. Subsequent reactions of $\text{CH}_3\text{S}(\text{O})_2\text{C}^{\bullet}\text{H}_2$

As described above, the energetics results suggested that the atmospheric transformation of $\text{DMS}(\text{O})_2$ that is initiated by OH radical, Cl atom, and NO_3 radical proceeds via H-atom abstraction from the methyl group to form $\text{CH}_3\text{S}(\text{O})_2\text{C}^{\bullet}\text{H}_2$ as a major product. Under tropospheric conditions, it is anticipated that the removal process for this radical could involve self-dissociation and/or its reaction with molecular oxygen ($^3\text{O}_2$). We performed calculations to optimize the relevant geometries and corresponding harmonic vibrational frequency calculations for all of the stationary points involved in the self-dissociation of $\text{CH}_3\text{S}(\text{O})_2\text{C}^{\bullet}\text{H}_2$, as well as the H-atom abstraction and addition paths of the $\text{CH}_3\text{S}(\text{O})_2\text{C}^{\bullet}\text{H}_2 + ^3\text{O}_2$ reaction at the same M06-2X/aug-cc-pV(T+d)Z level used for the other calculations in this work. Single point energy calculations for all the stationary points were performed at the CCSD(T)/aug-cc-pV(T+d)Z level on the M06-2X level-optimized geometries. The self-dissociation of $\text{CH}_3\text{S}(\text{O})_2\text{C}^{\bullet}\text{H}_2$ leading to the formation of sulfene ($\text{CH}_2=\text{S}(\text{O})_2$) + methyl radical ($^{\bullet}\text{CH}_3$) products is shown in eqn. 3 and the corresponding PES profile is shown in Fig. S3. In Fig. S3, the relative energies and Gibbs free energies are shown without and with parentheses, respectively, and correspond to values computed at the CCSD(T)/aug-cc-pV(T+d)Z//M06-2X/aug-cc-pV(T+d)Z level. The PES profile for this reaction proceeds through the stationary points TS10 and PC10, which then lead to products (sulfene + methyl radical). The barrier height and Gibbs free energy barrier for this reaction was found to be ~ 35.9 kcal mol $^{-1}$ (see Fig. S3). The high barrier height and Gibbs free energy barrier for the self-dissociation of $\text{CH}_3\text{S}(\text{O})_2\text{C}^{\bullet}\text{H}_2$ indicate that it is not energetically feasible under tropospheric conditions.



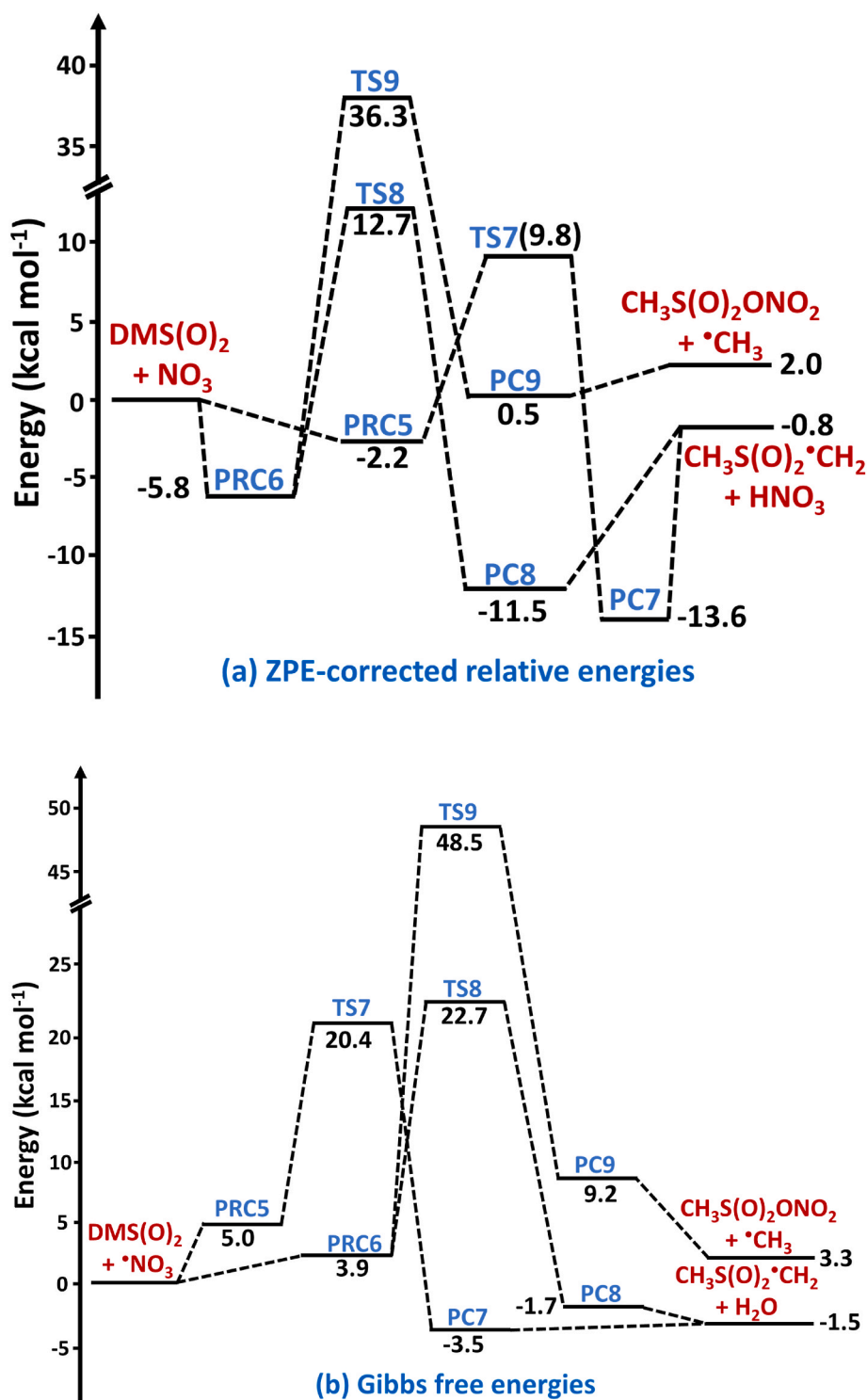


Fig. 4. The CCSD(T)/aug-cc-pV(T+d)Z//M06-2X/aug-cc-pV(T+d)Z level calculated: (a) ZPE-corrected relative energies; and (b) Gibbs free energy profiles for the abstraction and substitution paths involving DMS(O)₂ + NO₃ radical to form their respective products. The symbols PRC5 and PRC6; TS7, TS8, and TS9; and PC7, PC8 and PC9; refer to pre-reactive complexes; transition states; and post-reactive complexes respectively.

3.3. PES profiles for the CH₃S(O)₂C•H₂ + ³O₂ reaction

The zero point corrected CCSD(T)//M06-2X level calculated potential energy profiles and Gibbs free energy profiles calculated at the CCSD (T)//M06-2X level for the abstraction channels associated with the CH₃S(O)₂C•H₂ + ³O₂ reaction are shown in Fig. 5 and Fig. S4, respectively. The results in Fig. 5 show that abstraction of an H-atom from the -CH₂ group by molecular oxygen proceeds via TS11 with a barrier height

of 57.1 kcal mol⁻¹ to form PC11, which leads to the formation of CH₃S(O)₂C•H (P1) + HO₂ radical. On the other hand, although all three of its hydrogens are attached to the same carbon atom, two distinct H-abstraction transition states are possible for the methyl group H-atoms. This is because two of the methyl group hydrogens are oriented towards the two oxygens of the S(O)₂ group, with the third oriented away from it. Therefore, two different transition states are possible. Accordingly, H-atom abstraction from the methyl group by O₂

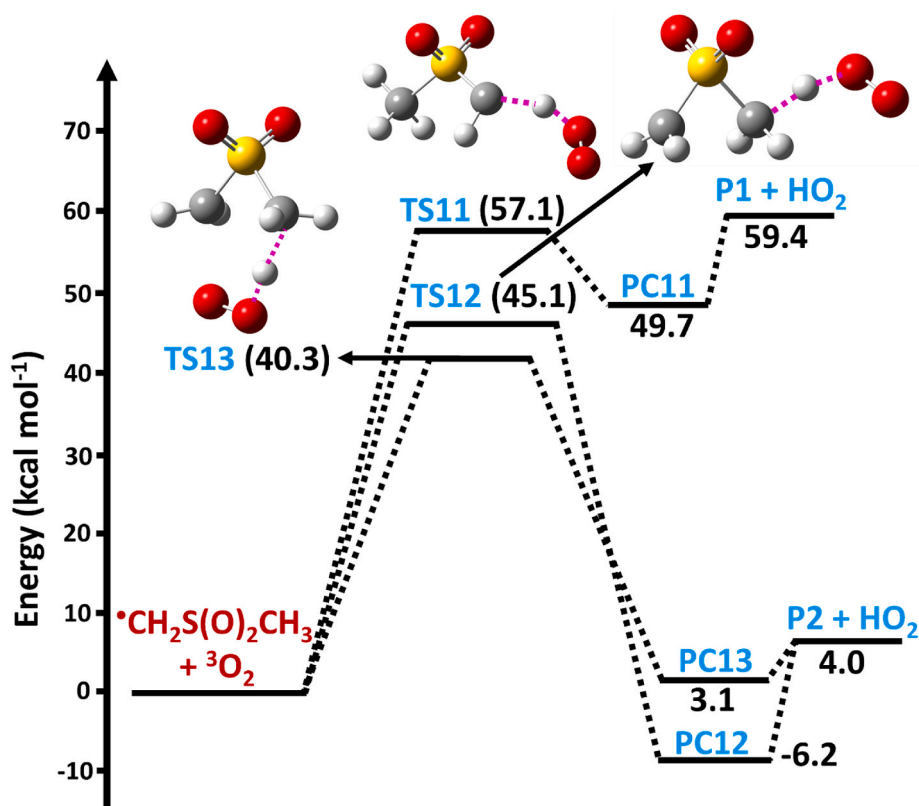


Fig. 5. The potential energy diagram for the three possible H-atom abstraction paths involved in the $\text{CH}_3\text{S}(\text{O})_2\text{C}^*\text{H}_2 + {}^3\text{O}_2$ reaction, obtained at the CCSD(T)/aug-cc-pV(T+d)Z//M06-2X/aug-cc-pV(T+d)Z level. The symbols TS11, TS12, and TS13; and PC11, PC12, and PC13; and P₁ and P₂; represent transition states; product complexes; and products respectively.

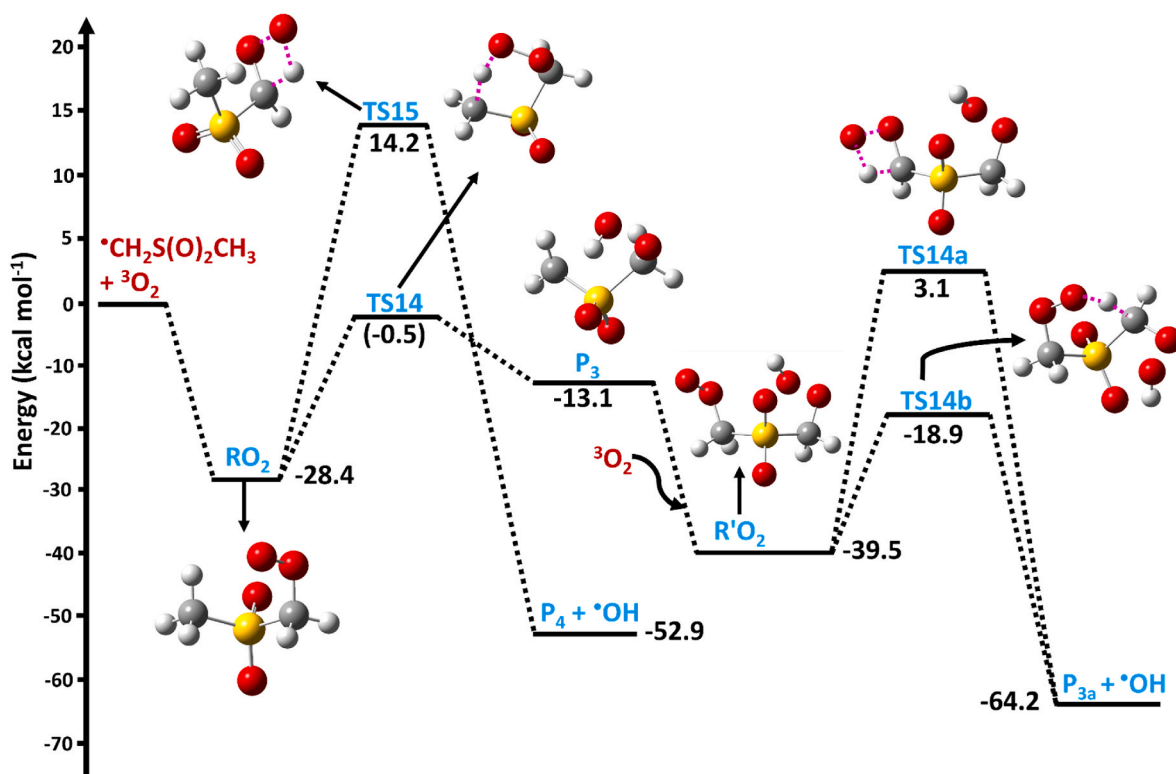


Fig. 6. The CCSD(T)/aug-cc-pV(T+d)Z//M06-2X/aug-cc-pV(T+d)Z level calculated potential energy profiles for the $\text{CH}_3\text{S}(\text{O})_2\text{C}^*\text{H}_2 + {}^3\text{O}_2$ reaction leading to formation of various products. The symbol RO₂ represents the $\text{CH}_3\text{S}(\text{O})_2\text{CH}_2\text{OO}^\bullet$ radical adduct; TS14, TS14a, TS14b and TS15 represent transition states; and P₃ ($\text{CH}_3\text{S}(\text{O})_2\text{CH}_2\text{OOH}$), P_{3a} ($\text{HC}(\text{O})\text{S}(\text{O})_2\text{CH}_2\text{OOH}$), and P₄ ($\text{CH}_3\text{S}(\text{O})_2\text{C}(\text{O})\text{H}$) represent products.

through TS12 and TS13 to form the corresponding PC12 and PC13 can occur, leading to formation of the same cyc-C₂H₂SO₂ (P₂) + HO₂ products on the PES (at 4.0 kcal mol⁻¹). The barrier heights for TS12 and TS13 using the present level of calculations were computed to be 45.1 and 40.3 kcal mol⁻¹. From Fig. S4, the Gibbs free energy barriers for TS11, TS12 and TS13 were computed to be 65.9, 54.5, and 51.4 kcal mol⁻¹ at the CCSD(T)/M06-2X level. These reaction barriers and Gibbs free energy barriers are too high to be achievable under tropospheric conditions. Therefore, we did not consider these three abstraction paths for any further kinetics calculations, and have performed the calculations only for the sake of completeness.

The reaction of CH₃S(O)₂C*H₂ + ³O₂ can also proceed through an addition mechanism as previously mentioned. The zero point corrected CCSD(T)/M06-2X level computed PES profile and Gibbs free energy profiles calculated at the CCSD(T)/M06-2X level for the addition of oxygen to the C-atom of CH₃S(O)₂C*H₂ are shown in Fig. 6 and Fig. S5, respectively. Initially, atmospheric ³O₂ attacks the C-centered radical carbon of CH₃S(O)₂C*H₂ to form a stable barrierless CH₃S(O)₂CH₂OO* adduct (i.e., RO₂, where R = CH₃S(O)₂CH₂) with an energy that is 28.4 kcal mol⁻¹ below the CH₃S(O)₂C*H₂ + O₂ separated reactants. We first performed calculations to determine the more stable conformer of this RO₂ adduct. The process revealed a total of about 26 conformations, the most stable of which is shown in Fig. 6 (located at -28.4 kcal mol⁻¹ on the PES). This excess energy can facilitate further subsequent reactions of this radical such as intramolecular hydrogen shifts, elimination reactions, or the reverse reaction leading back to the starting CH₃S(O)₂C*H₂ + ³O₂ reactants. We note that the binding energy for this CH₃S(O)₂CH₂OO* adduct is in close agreement with the value for the NH₂S(O)₂CH₂OO* adduct formed from addition of O₂ to NH₂S(O)₂C*H₂ (reported to be -27.8 kcal mol⁻¹ using the same computational level (Arathala and Musah, 2023)). In addition, we found that CH₃S(O)₂CH₂OO* was less stable by ~1.2 kcal mol⁻¹ when compared to the value for the CH₃S(O)CH₂OO* adduct. The reported binding energy for the CH₃S(O)CH₂OO* adduct was -29.6 kcal mol⁻¹ at the CBS-QB3 level (Asatryan and Bozzelli, 2008). From Fig. 6 and Fig. S5, it can be seen that an intramolecular hydrogen shift from the methyl group to the terminal oxygen atom of the peroxy radical through TS14 leads to a QOOH radical product (P₃; where Q = *CH₂S(O)₂CH₂OOH) with a barrier height of -0.5 kcal mol⁻¹ and a Gibbs free energy barrier of 11.3 kcal mol⁻¹. It is expected that the formed QOOH radical will further react with a second molecular oxygen (³O₂) under tropospheric conditions to produce a stable R'O₂ radical (where R' = HOOCH₂S(O)₂CH₂OO*) with an energy of -26.4 kcal mol⁻¹ below the QOOH (P₃) + O₂ separated reactants. It further undergoes OH radical elimination through a concerted mechanism via TS14a and a hydrogen atom shift from the -CH₂ group to the terminal O-atom of R'O₂ via TS14b, to produce products P3a (HC(O)S(O)₂CH₂OOH) + OH radical) with corresponding barrier heights of 3.1 and -18.9 kcal mol⁻¹, and corresponding Gibbs free energy barriers of 24.6 and 3.8 kcal mol⁻¹ respectively, relative to the energy of starting separated CH₃S(O)₂C*H₂ + ³O₂ reactants. The reaction that proceeds via TS14a to form products P3a + OH radical is not expected to be an important process. However, an intramolecular hydrogen shift via TS14b to produce products P3a + OH radical may be important, since the barrier height for this reaction path is ~22 kcal mol⁻¹ lower compared to the OH radical elimination path that proceeds via TS14a (see Fig. 6).

It was also found that the RO₂ radical undergoes a concerted elimination process involving C-H and O-O single bond rupture, followed by simultaneous double bond formation between the C- and O-atoms via TS15 (see the structure of TS15 in Fig. 6) leading to CH₃S(O)₂C(O)H (P₄) + *OH with a barrier of ~14.2 kcal mol⁻¹ and a Gibbs free energy barrier of 25.3 kcal mol⁻¹ above the starting CH₃S(O)₂C*H₂ + ³O₂ separated reactants. Based on the results, the reaction of CH₃S(O)₂C*H₂ + ³O₂ proceeds first by O₂ addition, followed by two hydrogen atom shift reaction steps (i.e., RO₂ → TS14 → QOOH (P₃)); and R'O₂ → TS14b → HC(O)S(O)₂CH₂OOH (P3a) + OH radical). These paths may be important processes under tropospheric conditions.

4. Theoretical kinetic analysis

Rate coefficient calculations were performed for the abstraction paths involved in the DMS(O)₂ + *OH; DMS(O)₂ + *Cl; and DMS(O)₂ + NO₃* reactions, and the subsequent reaction of CH₃S(O)₂C*H₂ with ³O₂, using the Master equation solver for multi-energy well reactions (Mesmer v5.2) software (Glowacki et al., 2012). The form of the energy-grained master equation used in this work by the Mesmer code is discussed in detail in our previous work (Arathala and Musah, 2019) and in various studies reported by other groups (Glowacki et al., 2012; Parandaman et al., 2018; Piletic et al., 2017). Basically, the energy of the isomer adducts on the PESs are divided into grains that are used as the basis of the chemical master equation model. The form of the energy-grained master equation used in this work is given in eq (4).

$$\frac{d}{dt} \mathbf{p} = \mathbf{M} \mathbf{p} \quad (4)$$

In eq (4), the symbol **p** is a vector containing the populations, and the symbol **M** is a matrix that determines the grain population evaluation due to collisional energy transfer. The collisional energy transfer is described using an exponential down model. The zero point corrected energies for all of the stationary points on the PESs (see Figs. 2a and 3a, 4a and 6), rotational constants and vibrational frequencies were taken from the present calculations to provide input for the Mesmer rate calculations.

The single exponential down model with an average transfer energy of ΔE_d = 200 cm⁻¹ was used to simulate the collision energy transfer between the intermediates (PRCs and PCs) and bath gas (N₂) for the reactions involving DMS(O)₂ with *OH/*Cl/NO₃* as well as for the CH₃S(O)₂C*H₂ + ³O₂ reaction. This value was chosen based on the observation of similar reactions reported in the literature that used the presently studied atmospheric oxidants (Bunkan et al., 2015; Hyttinen et al., 2016; Ma et al., 2018; Parandaman et al., 2018; Xie et al., 2015). Lennard-Jones (L-J) interaction potentials were also required for calculating the collision frequencies. Therefore, we used the L-J parameters provided in Table S6 for the PRCs and PCs involved in the DMS(O)₂ + *OH/*Cl/NO₃* reactions, as well as for the RO₂ radical adduct involved in the CH₃S(O)₂C*H₂ + ³O₂ reaction. The L-J parameters for the various complexes and the RO₂ radical adduct were based on those of the nearest sized alkane (Jasper and Miller, 2014) and for the bath gas, N₂ was used in the calculations with the corresponding L-J parameters of σ = 3.9 Å and ε = 48 K (Glowacki et al., 2012).

For the reactions of DMS(O)₂ + *OH/*Cl/NO₃*, as well as for the CH₃S(O)₂C*H₂ + ³O₂ reaction, RRKM theory was used to calculate microcanonical rate coefficients for the reaction steps that proceed through a transition state with a well defined barrier (Glowacki et al., 2012). To account for the impact of tunneling on the reaction rates, the Eckart tunneling correction was used (Miller, 1979). As shown previously for the interaction of a structural analog of DMS(O)₂ (i.e., methane sulfonamide (MSAM)) with *OH/*Cl/NO₃* (Arathala and Musah, 2022, 2023), the reaction of CH₃S(O)₂C*H₂ with ³O₂ to form the corresponding complexes is a barrierless process. Accordingly, we used the Inverse Laplace Transform (ILT) method implemented in Mesmer for barrierless reactions (Glowacki et al., 2012). The Arrhenius pre-exponential factor used in the ILT approach for the DMS(O)₂ + *OH/*Cl/NO₃* and CH₃S(O)₂C*H₂ + O₂ barrierless reactions was 1.0 × 10⁻¹¹ cm³ molecule⁻¹ s⁻¹ (see Figs. 2a, 3a and 4a, and 6). We set a value of 0 kcal mol⁻¹ for the activation energy and a value of 0.1 for the modified Arrhenius parameter for all the barrierless reaction paths that were used to calculate rate coefficients in the present work.

The simulated reaction profiles provided in the Mesmer calculations were treated according to the logarithmic transformation of the pseudo-first order reaction rate law as given in eqn. (5).

$$\ln \left(\frac{[X]}{[X]_0} \right) = -k't \quad (5)$$

In eqn. (5), the symbol k' is the pseudo-first order rate coefficient and X is the deficient reactant for the respective reaction. Plotting the above equation from the beginning of the simulation until the total consumption of the deficient reactant showed linear trends for all the title reactions. The bimolecular reaction rate coefficient was estimated by dividing the slope of the linear fit (k') with the concentration of the excess reactant. For the reactions involving $\text{DMS}(\text{O})_2 + ^\bullet\text{OH}$, $\text{DMS}(\text{O})_2 + ^\bullet\text{Cl}$, and $\text{DMS}(\text{O})_2 + \text{NO}_3^\bullet$, the reactant $\text{DMS}(\text{O})_2$ was assumed to have a larger concentration relative to oxidants such as $^\bullet\text{OH}$, $^\bullet\text{Cl}$, and NO_3^\bullet under atmospheric conditions. In the case of the $\text{CH}_3\text{S}(\text{O})_2\text{C}^\bullet\text{H}_2 + ^3\text{O}_2$ reaction, the concentration of $^3\text{O}_2$ in the atmosphere is in significant excess compared to that of $\text{CH}_3\text{S}(\text{O})_2\text{C}^\bullet\text{H}_2$. Thus, in the present calculations, $^3\text{O}_2$ and $\text{CH}_3\text{S}(\text{O})_2\text{C}^\bullet\text{H}_2$ were treated as excess and deficient reactants respectively.

4.1. Kinetics

Using all the required parameters provided in the theoretical kinetic analysis section of the Mesmer kinetic code, we obtained the rate coefficients for the two possible H-abstraction paths involved in the reactions of $\text{DMS}(\text{O})_2 + ^\bullet\text{OH}$; $\text{DMS}(\text{O})_2 + ^\bullet\text{Cl}$; and $\text{DMS}(\text{O})_2 + \text{NO}_3^\bullet$ in the temperature range of 200–320 K and at 1 atm pressure (which are relevant to tropospheric conditions). The results are displayed in Table 1. The rate coefficient values in this temperature range can be helpful for atmospheric modeling calculations that can be useful for evaluation of atmospheric lifetimes. The computed rate coefficients for the reaction of $\text{DMS}(\text{O})_2 + \text{OH}$ radical indicate that the H-atom abstraction by OH radical via TS1 is ~1–2 orders of magnitude larger than the same reaction via TS2 in the temperatures between 200 and 320 K. For example, the calculated rate coefficients via TS1 and TS2 at 298 K were found to be 4.5×10^{-13} and 1.1×10^{-14} $\text{cm}^3 \text{ molecule}^{-1} \text{ s}^{-1}$, respectively. The rate coefficients for the H-abstraction via TS4 associated with the $\text{DMS}(\text{O})_2 + \text{Cl}$ atom reaction was predicted to be 2–4 orders of magnitude larger compared to H-abstraction via TS5 in the temperature range between 200 and 320 K. The obtained site specific H-abstraction rate coefficient via TS4 at 298 K was found to be 9.1×10^{-14} $\text{cm}^3 \text{ molecule}^{-1} \text{ s}^{-1}$, which is ~2 orders of magnitude larger, compared to the value for TS5, whose rate coefficient was found to be 1.3×10^{-16} $\text{cm}^3 \text{ molecule}^{-1} \text{ s}^{-1}$ at the same temperature. Similarly, the rate coefficient for the abstraction path associated with the $\text{DMS}(\text{O})_2 + \text{NO}_3^\bullet$ radical reaction via TS7 was calculated to be ~2 orders of magnitude larger compared to the values of the same reaction via TS8 in the present studied temperature range. For example, at 298 K, the estimated rate coefficient for the H-abstraction path via TS7 and TS8 respectively were

found to be 3.7×10^{-15} and 2.2×10^{-17} $\text{cm}^3 \text{ molecule}^{-1} \text{ s}^{-1}$.

The data in Table 1 were plotted to show the comparison between the different site-specific rate coefficients as a function of temperature for the $\text{DMS}(\text{O})_2 + ^\bullet\text{OH}$, $\text{DMS}(\text{O})_2 + ^\bullet\text{Cl}$ and $\text{DMS}(\text{O})_2 + \text{NO}_3^\bullet$ reactions (see Fig. 7). The results in Fig. 7 show that the rate coefficient trend for the $\text{DMS}(\text{O})_2 + ^\bullet\text{OH}$ reaction via TS1 exhibits a negative temperature dependence (i.e., the rate coefficient decreases with increasing temperature). Via TS2, it was found to exhibit a positive temperature dependence (i.e., the rate coefficient increased with increasing temperature) in the studied temperature range. The rate coefficient trend for the $\text{DMS}(\text{O})_2 + ^\bullet\text{Cl}$ reaction through TS4 was found to be slightly curved, with a negative temperature dependence above 200 K and a positive temperature dependence above 240 K. However, in the case of TS5, a positive temperature dependence was observed throughout the range of studied temperatures. The results also indicate that the variation of the rate coefficients with temperature for the $\text{DMS}(\text{O})_2 + \text{NO}_3^\bullet$ reactions via TS7 and TS8 was almost independent of temperature.

We estimated the overall rate coefficients for the $\text{DMS}(\text{O})_2 + \text{OH}$ radical, $\text{DMS}(\text{O})_2 + \text{Cl}$ atom, and $\text{DMS}(\text{O})_2 + \text{NO}_3^\bullet$ radical reactions for the site specific hydrogen abstraction channels in the studied temperature range (eqns (6)–(8)).

$$k_{\text{total}}^{\text{OH}} = k_{\text{TS1}} + k_{\text{TS2}} \quad (6)$$

$$k_{\text{total}}^{\text{Cl}} = k_{\text{TS4}} + k_{\text{TS5}} \quad (7)$$

$$k_{\text{total}}^{\text{NO}_3} = k_{\text{TS7}} + k_{\text{TS8}} \quad (8)$$

In eqns (6)–(8), $k_{\text{total}}^{\text{OH}}$, $k_{\text{total}}^{\text{Cl}}$, and $k_{\text{total}}^{\text{NO}_3}$ are the overall rate coefficients for the reactions of $\text{DMS}(\text{O})_2 + \text{OH}$ radical, $\text{DMS}(\text{O})_2 + \text{Cl}$ atom, and $\text{DMS}(\text{O})_2 + \text{NO}_3^\bullet$ radical, respectively. The symbols k_{TS1} , k_{TS2} , k_{TS4} , k_{TS5} , k_{TS7} and k_{TS8} are the individual H-atom abstraction path rate coefficients associated with TS1, TS2, TS4, TS5, TS7 and TS8, respectively. The obtained overall rate coefficients for the present three title reactions are provided in Table 1 and plotted in Fig. 7. The results indicate that the overall rate coefficients for the reaction of $\text{DMS}(\text{O})_2$ with OH radical decreases with increasing temperature in the presently studied temperature range. The calculated overall rate coefficient for the $\text{DMS}(\text{O})_2 + \text{OH}$ radical at 298 K was found to be 4.6×10^{-13} $\text{cm}^3 \text{ molecule}^{-1} \text{ s}^{-1}$, which agrees reasonably with the experimentally determined rate coefficient (3.0×10^{-13} $\text{cm}^3 \text{ molecule}^{-1} \text{ s}^{-1}$) at the same temperature (Falbe-Hansen et al., 2000). The overall rate coefficients for the reaction of $\text{DMS}(\text{O})_2 + \text{Cl}$ atom in the studied temperature range were found to increase with increasing temperature. For example, at 200 and 320 K, the overall rate coefficients for this reaction were found to be

Table 1

Rate coefficients for the H-abstraction channels and the overall reaction of $\text{DMS}(\text{O})_2 + ^\bullet\text{OH}$; $\text{DMS}(\text{O})_2 + ^\bullet\text{Cl}$; and $\text{DMS}(\text{O})_2 + \text{NO}_3^\bullet$ in the temperature range between 200 and 320 K and 1 atm pressure.^a

T (K)	$\text{DMS}(\text{O})_2 + \text{OH}$ radical			$\text{DMS}(\text{O})_2 + \text{Cl}$ atom			$\text{DMS}(\text{O})_2 + \text{NO}_3^\bullet$ radical		
	TS1 ^b	TS2	$k(\text{OH})^c$	TS4 ^b	TS5	$k(\text{Cl})^c$	TS7 ^b	TS8	$k(\text{NO}_3)^c$
200	2.55×10^{-12}	1.63×10^{-14}	2.56×10^{-12}	8.41×10^{-14}	1.34×10^{-18}	8.41×10^{-14}	3.52×10^{-15}	2.74×10^{-17}	3.55×10^{-15}
220	1.69×10^{-12}	1.44×10^{-14}	1.71×10^{-12}	7.26×10^{-14}	4.00×10^{-18}	7.26×10^{-14}	3.53×10^{-15}	2.66×10^{-17}	3.56×10^{-15}
240	1.14×10^{-12}	1.29×10^{-14}	1.16×10^{-12}	6.90×10^{-14}	1.10×10^{-17}	6.90×10^{-14}	3.55×10^{-15}	2.56×10^{-17}	3.58×10^{-15}
250	9.51×10^{-13}	1.23×10^{-14}	9.64×10^{-13}	6.94×10^{-14}	1.78×10^{-17}	6.95×10^{-14}	3.57×10^{-15}	2.50×10^{-17}	3.59×10^{-15}
260	7.98×10^{-13}	1.18×10^{-14}	8.10×10^{-13}	7.12×10^{-14}	2.81×10^{-17}	7.12×10^{-14}	3.59×10^{-15}	2.43×10^{-17}	3.61×10^{-15}
280	5.78×10^{-13}	1.10×10^{-14}	5.89×10^{-13}	7.88×10^{-14}	6.63×10^{-17}	7.89×10^{-14}	3.63×10^{-15}	2.30×10^{-17}	3.65×10^{-15}
298	4.48×10^{-13}	1.07×10^{-14}	4.59×10^{-13}	9.06×10^{-14}	1.34×10^{-16}	9.08×10^{-14}	3.67×10^{-15}	2.17×10^{-17}	3.69×10^{-15}
300	4.37×10^{-13}	1.07×10^{-14}	4.47×10^{-13}	9.23×10^{-14}	1.45×10^{-16}	9.24×10^{-14}	3.67×10^{-15}	2.16×10^{-17}	3.70×10^{-15}
320	3.43×10^{-13}	1.06×10^{-14}	3.54×10^{-13}	1.13×10^{-13}	2.95×10^{-16}	1.13×10^{-13}	3.73×10^{-15}	2.04×10^{-17}	3.75×10^{-15}

^a All rate coefficients are in units of $\text{cm}^3 \text{ molecule}^{-1} \text{ s}^{-1}$.

^b The degeneracy of TS1, TS4, and TS7 is 2 and hence the rate coefficients for these TSs were multiplied by 2.

^c $k(\text{OH})$, $k(\text{Cl})$, and $k(\text{NO}_3)$ are the overall rate coefficients for the $\text{DMS}(\text{O})_2 + \text{OH}$ radical; $\text{DMS}(\text{O})_2 + \text{Cl}$ atom; and $\text{DMS}(\text{O})_2 + \text{NO}_3^\bullet$ radical reactions respectively, obtained by adding the corresponding site-specific rate coefficients at each temperature.

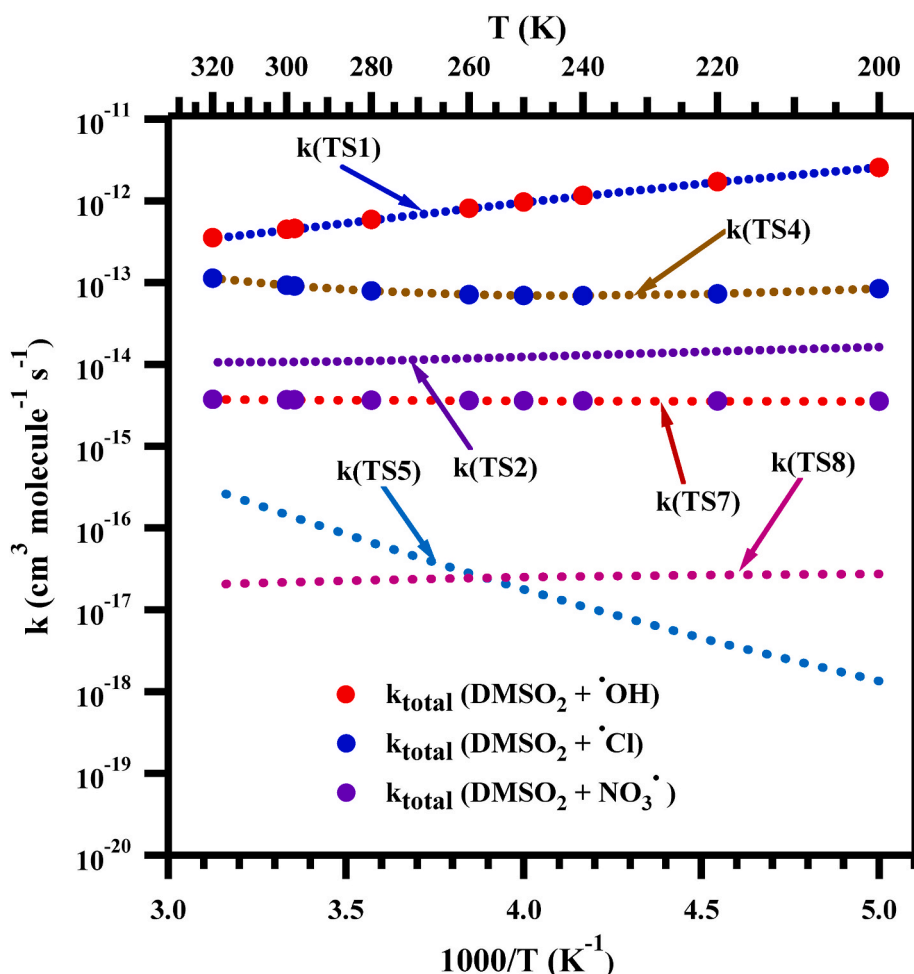


Fig. 7. Comparison between the calculated site-specific rate coefficients and the overall rate coefficients for the $\text{DMS}(\text{O})_2 + \cdot\text{OH}$, $\text{DMS}(\text{O})_2 + \cdot\text{Cl}$ and $\text{DMS}(\text{O})_2 + \text{NO}_3\cdot$ reactions over the temperature range of 200–320 K and at 1 atm pressure. The symbols $k(\text{TS1})$, $k(\text{TS2})$, $k(\text{TS4})$, $k(\text{TS5})$, $k(\text{TS7})$ and $k(\text{TS8})$ are the rate coefficients for the individual H-atom abstraction paths associated with TS1, TS2, TS4, TS5, TS7 and TS8, respectively.

8.4×10^{-14} and $1.1 \times 10^{-13} \text{ cm}^3 \text{ molecule}^{-1} \text{ s}^{-1}$, respectively. The rate coefficient for this reaction at 298 K was reported to be $(2.4 \pm 0.8) \times 10^{-14} \text{ cm}^3 \text{ molecule}^{-1} \text{ s}^{-1}$, which is ~ 4 times smaller compared to the value of the present calculated rate coefficient ($9.1 \times 10^{-14} \text{ cm}^3 \text{ molecule}^{-1} \text{ s}^{-1}$) at the same temperature (Falbe-Hansen et al., 2000). In addition, the overall rate coefficient results for the reaction of $\text{DMS}(\text{O})_2 + \text{NO}_3\cdot$ radical suggest that they are independent of temperature in the present studied temperature range. For example, the obtained overall rate coefficients for this reaction at 200 and 300 K were found to be 3.6×10^{-15} and $3.7 \times 10^{-15} \text{ cm}^3 \text{ molecule}^{-1} \text{ s}^{-1}$, respectively. Also, the overall rate coefficient obtained at 298 K for this reaction agrees with the previously reported value ($2.0 \times 10^{-15} \text{ cm}^3 \text{ molecule}^{-1} \text{ s}^{-1}$) (Falbe-Hansen et al., 2000). The rate coefficient data in Table 1 suggest that OH radical is more reactive than the Cl atom and $\text{NO}_3\cdot$ radical for the oxidation of $\text{DMS}(\text{O})_2$ in the temperatures between 200 and 320 K.

It is important to compare the results obtained at the M06-2X level to those obtained using the CCSD(T)/M06-2X level, because the results reported at the M06-2X level sometimes exhibit better agreement with experimental data than those acquired at the higher CCSD(T) level (Zavala-Oseguera et al., 2009). Thus, at the M06-2X/aug-cc-pV(T+d)Z level, we calculated the rate coefficients using the energies of all the stationary points for the abstraction paths associated with the $\text{DMS}(\text{O})_2 + \cdot\text{OH}$, $\text{DMS}(\text{O})_2 + \cdot\text{Cl}$, and $\text{DMS}(\text{O})_2 + \text{NO}_3\cdot$ reactions (see Table S7). In this regard, the same methodology described in the theoretical kinetic analysis section for estimating the rate coefficients using M06-2X calculated energies was used. The obtained rate coefficients (in cm^3

$\text{molecule}^{-1} \text{ s}^{-1}$) for each site-specific reaction, as well as the overall reaction rate coefficients in the temperature range of 200–320 K and at 1 atm pressure for the title reactions are displayed in Table S8. The results indicate that the trend in rate coefficients for all site-specific reactions and the overall title reactions were similar to those obtained using the CCSD(T)/M06-2X level calculated energies.

To gain further insights from the rate coefficients obtained using energies computed at various levels, we compared the overall rate coefficients obtained using the M06-2X and CCSD(T)/M06-2X approaches with the experimentally reported rate coefficients for the title reactions. The overall rate coefficients for the $\text{DMS}(\text{O})_2 + \cdot\text{OH}$ reaction using the M06-2X level were found to be ~ 2 times larger than the values obtained at the CCSD(T)/M06-2X level in the temperatures between 200 and 320 K. For example, the overall rate coefficients for this reaction at 298 K for the M06-2X and CCSD(T)/M06-2X levels were found to be 1.2×10^{-12} and $4.6 \times 10^{-13} \text{ cm}^3 \text{ molecule}^{-1} \text{ s}^{-1}$, respectively. The results also suggest that the overall rate coefficient for this reaction at 298 K using the M06-2X level is ~ 4 times larger than the experimentally reported one ($3.0 \times 10^{-13} \text{ cm}^3 \text{ molecule}^{-1} \text{ s}^{-1}$) at the same temperature.

In the case of the $\text{DMS}(\text{O})_2 + \cdot\text{Cl}$ reaction, the overall rate coefficient calculated at the M06-2X level is ~ 3 –8 times larger than the values obtained at the CCSD(T)/M06-2X level in the present studied temperature range. For example, the overall rate coefficient obtained using M06-2X at 298 K was found to be $2.9 \times 10^{-13} \text{ cm}^3 \text{ molecule}^{-1} \text{ s}^{-1}$, which is ~ 3 times larger than the value obtained at the CCSD(T)/M06-2X level ($9.1 \times 10^{-14} \text{ cm}^3 \text{ molecule}^{-1} \text{ s}^{-1}$) and ~ 12 times larger than

the reported experimentally obtained value ($2.4 \times 10^{-14} \text{ cm}^3 \text{ molecule}^{-1} \text{ s}^{-1}$) at the same temperature.

In addition, we also compared the overall rate coefficient for the $\text{DMS}(\text{O})_2 + \text{NO}_3^\bullet$ reaction at the M06-2X level with the value computed at the CCSD(T)//M06-2X level. It is found that the values obtained at the M06-2X level agreed well with those obtained at the CCSD(T)//M06-2X level in the entire studied temperature range. For example, the overall rate coefficient calculated at the M06-2X and CCSD(T)//M06-2X levels at 298 K were found to be 2.2×10^{-15} and $3.7 \times 10^{-15} \text{ cm}^3 \text{ molecule}^{-1} \text{ s}^{-1}$, respectively. Also, the overall rate coefficient using the M06-2X level was found to be in good agreement with the experimentally determined value ($2.0 \times 10^{-15} \text{ cm}^3 \text{ molecule}^{-1} \text{ s}^{-1}$). In conclusion, the overall rate coefficients calculated using CCSD(T)//M06-2X energies agree well with the experimentally measured rate coefficients for the $\text{DMS}(\text{O})_2 + \text{OH}^\bullet$ and $\text{DMS}(\text{O})_2 + \text{Cl}^\bullet$ reactions, whereas in case of the $\text{DMS}(\text{O})_2 + \text{NO}_3^\bullet$ reaction, the overall rate coefficients obtained using both M06-2X and CCSD(T)//M06-2X level energies agreed with the experimentally reported value.

4.2. Atmospheric lifetime

Atmospheric transformation of any compound is governed by its photolysis, and/or its reactions mediated by OH^\bullet , Cl^\bullet , and NO_3^\bullet , as well as with ozone (O_3). However, the rates of photolysis and the reaction of $\text{DMS}(\text{O})_2$ with O_3 are expected to be slow, because the rates of these reactions for methane sulfonamide, a structural analog of $\text{DMS}(\text{O})_2$, have been shown to be slow under tropospheric conditions (Arathala and Musah, 2022; Berasategui et al., 2020a). Therefore, it was anticipated that these $\text{DMS}(\text{O})_2$ removal processes are a negligible sink in the troposphere, and that $\text{DMS}(\text{O})_2$ degradation mainly depends on its reactions with OH^\bullet , Cl^\bullet and NO_3^\bullet .

The lifetime of $\text{DMS}(\text{O})_2$ in the presence of OH^\bullet , Cl^\bullet and NO_3^\bullet under atmospheric conditions can be expressed using eqn. (9) (Kumar and Rajakumar, 2019; Kurylo and Orkin, 2003; Mishra et al., 2016):

$$\frac{1}{\tau_{\text{eff}}} = \frac{1}{\tau_{\text{OH}}} + \frac{1}{\tau_{\text{Cl}}} + \frac{1}{\tau_{\text{NO}_3}} \quad (9)$$

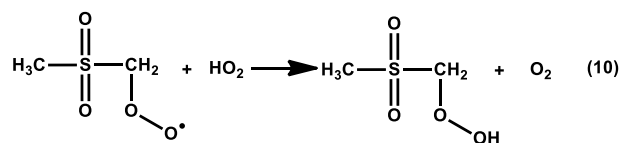
where τ_{eff} represents the cumulative atmospheric lifetime of the $\text{DMS}(\text{O})_2$ molecule. The symbols τ_{OH} , τ_{Cl} , and τ_{NO_3} represent the lifetimes of $\text{DMS}(\text{O})_2$ with respect to its reactions with OH^\bullet , Cl^\bullet and NO_3^\bullet , respectively. The present calculated rate coefficients for the reactions of $\text{DMS}(\text{O})_2$ with OH^\bullet , Cl^\bullet and NO_3^\bullet were estimated in the temperatures between 200 and 320 K (see Table 1), using concentrations of $[\text{OH}] = 1.0 \times 10^6 \text{ molecules cm}^{-3}$; $[\text{Cl}] = 1.3 \times 10^5 \text{ atoms cm}^{-3}$; and $[\text{NO}_3] = 5.0 \times 10^8 \text{ molecules cm}^{-3}$ for calculating the lifetime of $\text{DMS}(\text{O})_2$ (Atkinson, 2000; Logan, 1985; Rao et al., 2018; Spicer et al., 1998). The calculation results suggest that the lifetimes of $\text{DMS}(\text{O})_2$ with respect to its reactions with OH^\bullet , Cl^\bullet and NO_3^\bullet are 5–35, 5–1050, and 6–6.5 days, respectively in the temperature range between 200 and 320 K. The cumulative atmospheric lifetime (τ_{cum}) was estimated from the reactions of $\text{DMS}(\text{O})_2$ with OH^\bullet , Cl^\bullet and NO_3^\bullet using eqn. (9). In eqn. (9), the atmospheric lifetimes of $\text{DMS}(\text{O})_2$ with respect to its reactions with OH^\bullet , Cl^\bullet and NO_3^\bullet are defined as $\tau_{\text{OH}} = 1/(k_{\text{OH}}[\text{OH}])$, $\tau_{\text{Cl}} = 1/(k_{\text{Cl}}[\text{Cl}])$, and $\tau_{\text{NO}_3} = 1/(k_{\text{NO}_3}[\text{NO}_3])$, respectively. The symbols k_{OH} , k_{Cl} , and k_{NO_3} represent the overall rate coefficients calculated for the $\text{DMS}(\text{O})_2 + \text{OH}^\bullet$, $\text{DMS}(\text{O})_2 + \text{Cl}^\bullet$ and $\text{DMS}(\text{O})_2 + \text{NO}_3^\bullet$ reactions. The $[\text{OH}]$, $[\text{Cl}]$, and $[\text{NO}_3]$ represent the average atmospheric concentrations of OH^\bullet , Cl^\bullet and NO_3^\bullet . The τ_{cum} was calculated in the temperature range of 200–320 K. The overall rate coefficients estimated for the $\text{DMS}(\text{O})_2 + \text{OH}^\bullet$, $\text{DMS}(\text{O})_2 + \text{Cl}^\bullet$ and $\text{DMS}(\text{O})_2 + \text{NO}_3^\bullet$ reactions are given in Table 1, and the average atmospheric concentrations of OH^\bullet , Cl^\bullet and NO_3^\bullet radicals given above were used in the calculations. By combining all the contributions from the OH^\bullet , Cl^\bullet , and NO_3^\bullet reactions, the cumulative atmospheric lifetime of $\text{DMS}(\text{O})_2$ was found to be ~3–5 days in the present studied temperature range. This result suggests that the atmospheric lifetime of

the title molecule is very short in the studied temperature range and as such, its impact on global warming is negligible. However, the final products formed from the subsequent reactions of the initially formed $\text{CH}_3\text{S}(\text{O})_2\text{C}^\bullet\text{H}_2$ product with respect to its reactions with O_2 , may have significant effects on acid rain formation and climate change. Therefore, to gain more insights from the kinetics of this reaction, we performed rate coefficient calculations for the two different reaction paths accessible for the $\text{CH}_3\text{S}(\text{O})_2\text{C}^\bullet\text{H}_2 + {}^3\text{O}_2$ reaction under the same studied temperature range.

Mesmer kinetic code was used to calculate the rate coefficients for the $\text{CH}_3\text{S}(\text{O})_2\text{C}^\bullet\text{H}_2 + {}^3\text{O}_2$ reaction. Fig. 6 suggests that two reaction pathways are possible: $\text{CH}_3\text{S}(\text{O})_2\text{C}^\bullet\text{H}_2 + {}^3\text{O}_2 \leftrightarrow \text{RO}_2 \rightarrow \text{P}_3$; and $\text{CH}_3\text{S}(\text{O})_2\text{C}^\bullet\text{H}_2 + {}^3\text{O}_2 \leftrightarrow \text{RO}_2 \rightarrow \text{P}_4 + \text{OH}^\bullet$. We calculated the reaction rate coefficients for these two paths using Mesmer (Glowacki et al., 2012) in the temperature range of 200–300 K and at 1 atm. The obtained rate coefficients (in $\text{cm}^3 \text{ molecule}^{-1} \text{ s}^{-1}$) for the reactions proceeding via TS14 and TS15 to form their respective products P_3 and $\text{P}_4 + \text{OH}^\bullet$ radical are displayed in Table S9, and Fig. 8 shows how the rate coefficients for the $\text{CH}_3\text{S}(\text{O})_2\text{C}^\bullet\text{H}_2 + {}^3\text{O}_2 \rightarrow \text{P}_3$ ($\text{CH}_2\text{S}(\text{O})_2\text{CH}_2\text{OOH}$) reaction through TS14 and $\text{CH}_3\text{S}(\text{O})_2\text{C}^\bullet\text{H}_2 + {}^3\text{O}_2 \rightarrow \text{P}_4$ ($\text{CH}_3\text{S}(\text{O})_2\text{C}(\text{OH})\text{H} + \text{OH}^\bullet$) reaction through TS15 vary between 200 and 300 K. The results suggest that the formation of QOOH radical (P_3) through TS14 is ~11–13 orders of magnitude faster compared to the other path that leads to the formation of products $\text{P}_4 + \text{OH}^\bullet$ radical via TS15. For example, at 298 K, the rate coefficients calculated for the formation of QOOH radical and $\text{P}_4 + \text{OH}^\bullet$ radical from the $\text{CH}_3\text{S}(\text{O})_2\text{C}^\bullet\text{H}_2 + {}^3\text{O}_2$ reaction were estimated to be 9.00×10^{-12} and $4.3 \times 10^{-23} \text{ cm}^3 \text{ molecule}^{-1} \text{ s}^{-1}$, respectively. Thus, the present results indicate that the $\text{CH}_3\text{S}(\text{O})_2\text{C}^\bullet\text{H}_2 + {}^3\text{O}_2$ reaction mainly proceeds via formation of the QOOH radical (P_3) under atmospheric conditions, when compared to the other possible path leading to $\text{P}_4 + \text{OH}^\bullet$ radical.

To determine whether there might be competition between self-dissociation of $\text{CH}_3\text{S}(\text{O})_2\text{C}^\bullet\text{H}_2$ and the $\text{CH}_3\text{S}(\text{O})_2\text{C}^\bullet\text{H}_2 + {}^3\text{O}_2$ reaction, we calculated rate coefficient for the self-dissociation reaction of $\text{CH}_3\text{S}(\text{O})_2\text{C}^\bullet\text{H}_2$ provided in eqn. 3, for the corresponding PES profile (see Fig. S3) using Mesmer code (Glowacki et al., 2012). The rate coefficient for the self-dissociation of $\text{CH}_3\text{S}(\text{O})_2\text{C}^\bullet\text{H}_2$ to form sulfene + methyl radical was found to be $8.2 \times 10^{-16} \text{ s}^{-1}$ at 298 K. For comparison, we calculated the effective rate coefficient for the $\text{CH}_3\text{S}(\text{O})_2\text{C}^\bullet\text{H}_2 + {}^3\text{O}_2$ reaction by using its bimolecular rate coefficient and the average atmospheric concentration of O_2 at 298 K. The effective rate coefficient for the $\text{CH}_3\text{S}(\text{O})_2\text{C}^\bullet\text{H}_2 + {}^3\text{O}_2$ reaction was estimated to be $\sim 9.0 \times 10^6 \text{ s}^{-1}$. To compute this value, we used the calculated bimolecular rate coefficient determined in this work for the reaction of $\text{CH}_3\text{S}(\text{O})_2\text{C}^\bullet\text{H}_2 + {}^3\text{O}_2$ at 298 K ($9.0 \times 10^{-12} \text{ cm}^3 \text{ molecule}^{-1} \text{ s}^{-1}$) and a concentration of $[\text{O}_2] = \sim 1 \times 10^{18} \text{ molecules cm}^{-3}$ (Hyttinen et al., 2016). The results suggest that the $\text{O}_2 + \text{CH}_3\text{S}(\text{O})_2\text{C}^\bullet\text{H}_2$ reaction is almost 20 orders of magnitude faster than the self-dissociation of $\text{CH}_3\text{S}(\text{O})_2\text{C}^\bullet\text{H}_2$ at 298 K.

Several studies indicate that the important competitive pathways for the unimolecular degradation of RO_2 radicals are those associated with their reactions with HO_2 and NO radicals (Atkinson and Arey, 2003; Boyd et al., 2003; Fu et al., 2022; Orlando and Tyndall, 2012). Therefore, we considered the bimolecular reactions of $\text{CH}_3\text{S}(\text{O})_2\text{CH}_2\text{OO}^\bullet$ radical with both, leading to the formation of the corresponding hydroperoxide + O_2 and alkoxy radical + NO_2 products respectively (see eqns. 10 and 11).



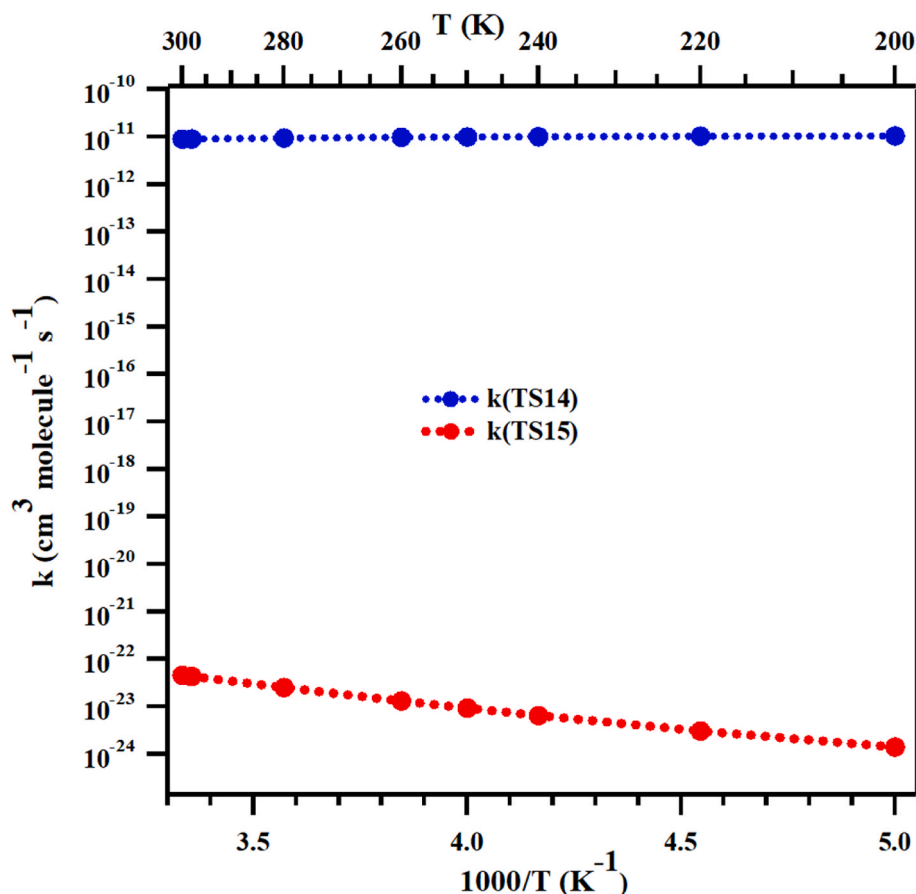
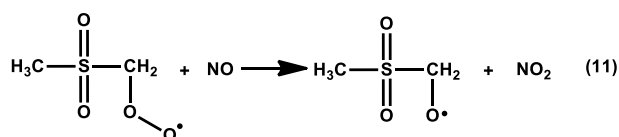


Fig. 8. Comparison of the rate coefficients ($\text{cm}^3 \text{ molecule}^{-1} \text{ s}^{-1}$) for the $\text{CH}_3\text{S}(\text{O})_2\text{C}^*\text{H}_2 + {}^3\text{O}_2 \rightarrow \text{P3}$ (${}^*\text{CH}_2\text{S}(\text{O})_2\text{CH}_2\text{OOH}$) reaction through TS14 and the $\text{CH}_3\text{S}(\text{O})_2\text{C}^*\text{H}_2 + {}^3\text{O}_2 \rightarrow \text{P4}$ ($\text{CH}_3\text{S}(\text{O})_2\text{C}(\text{O})\text{H}$) + ${}^*\text{OH}$ reaction through TS15 over the temperature range between 200 and 300 K.



The competition between the bimolecular and unimolecular reactions can be determined from the kinetics of these reactions. At 298 K, the rate coefficients for the typical $\text{RO}_2 + \text{HO}_2$ and $\text{RO}_2 + \text{NO}$ reactions are reported to be 1.7×10^{-11} and $1.2 \times 10^{-13} \text{ cm}^3 \text{ molecule}^{-1} \text{ s}^{-1}$ (Atkinson and Arey, 2003; Boyd et al., 2003). If the $\text{CH}_3\text{S}(\text{O})_2\text{CH}_2\text{OO}$ radical + HO_2 and $\text{CH}_3\text{S}(\text{O})_2\text{CH}_2\text{OO}$ radical + NO reactions are treated as pseudo-first order by considering the concentration of HO_2 and NO to be ~ 40 ppt and 100 ppt respectively (under urban atmospheric conditions in the afternoon, in indoor air and in remote areas) (Fu et al., 2022; Hofzumahaus et al., 2009; Lelieveld et al., 2008; Newland et al., 2021; Pagonis et al., 2019), then the obtained first order rate coefficients for the $\text{CH}_3\text{S}(\text{O})_2\text{CH}_2\text{OO}$ radical + HO_2 and $\text{CH}_3\text{S}(\text{O})_2\text{CH}_2\text{OO}$ radical + NO reactions are computed to be 0.017 and 0.02 s^{-1} , respectively. In addition, we calculated the first order rate coefficients for the RO_2 ($\text{CH}_3\text{S}(\text{O})_2\text{CH}_2\text{OO}$) radical isomerizations via TS14 and TS15, and found them to be 1.5×10^{-6} and $2.4 \times 10^{-14} \text{ s}^{-1}$, respectively. These results suggest that the bimolecular $\text{RO}_2 + \text{HO}_2$ and $\text{RO}_2 + \text{NO}$ reactions

are ~ 4 – 12 orders of magnitude faster than the corresponding unimolecular RO_2 isomerizations at high NO and HO_2 radical concentrations.

4.3. Reaction mechanism

Based on the aforementioned results and reactions reported in the literature, we propose a detailed mechanism for the atmospheric transformation of $\text{DMS}(\text{O})_2$ initiated by ${}^*\text{OH}/{}^*\text{Cl}/\text{NO}_3^*$ (presented in Fig. 9). The data from this work reveal that atmospheric ${}^*\text{OH}/{}^*\text{Cl}/\text{NO}_3^*$ abstract an H-atom from a methyl group of $\text{DMS}(\text{O})_2$ to form a C-centered $\text{DMS}(\text{O})_2$ radical and molecular water, HCl and HNO_3 respectively as primary reaction products. Under oxygen-rich conditions in the troposphere, the C-centered $\text{DMS}(\text{O})_2$ radical reacts with O_2 to produce the RO_2 (i.e., $\text{CH}_3\text{S}(\text{O})_2\text{CH}_2\text{OO}$) radical. This mechanism is illustrated with the black colored arrows in Fig. 9. The present energetics and rate results indicate that the RO_2 radical undergoes auto-oxidation via a hydrogen atom shift from the methyl group to the terminal O-atom, leading to formation of the QOOH radical (i.e., ${}^*\text{CH}_2\text{S}(\text{O})_2\text{CH}_2\text{OOH}$). This auto-oxidation mechanism is illustrated with red arrows in Fig. 9. The fate of the QOOH radical involves its reaction with another ${}^3\text{O}_2$ under tropospheric conditions to produce a $\text{R}'\text{O}_2$ radical (i.e., ${}^*\text{OOCH}_2\text{S}(\text{O})_2\text{CH}_2\text{OOH}$) adduct. The subsequent reaction of this $\text{R}'\text{O}_2$ radical was found to be transfer of a hydrogen atom from the $-\text{CH}_2$ group to the terminal O-atom of the $\text{R}'\text{O}_2$ radical to form

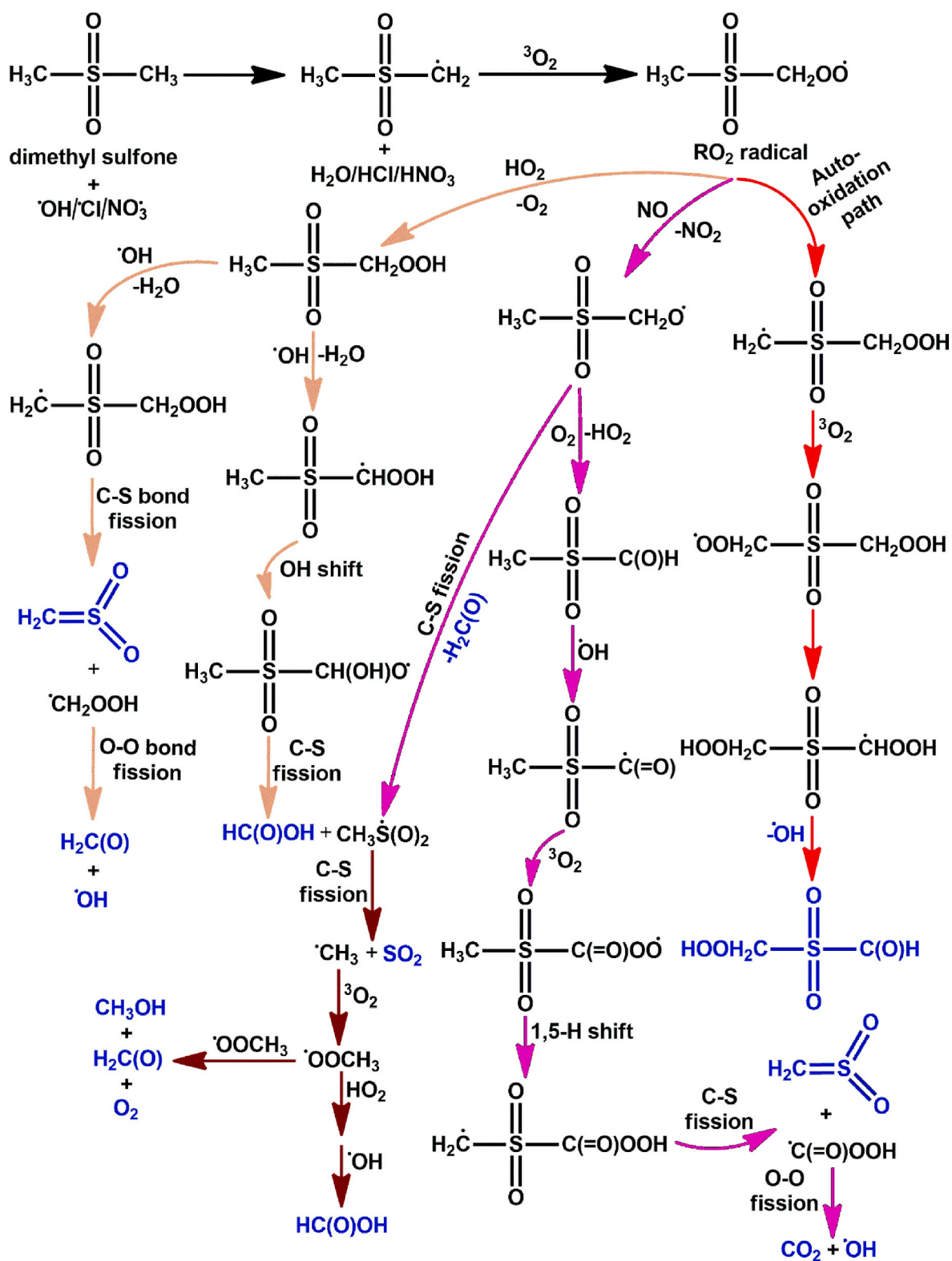
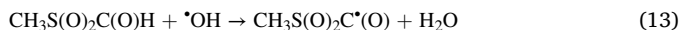
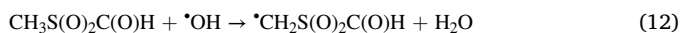


Fig. 9. Atmospheric oxidation mechanism for the reaction of DMS(O)₂ initiated by the [•]OH, NO₃[•] and [•]Cl, followed by subsequent reactions of CH₃S(O)₂C[•]H₂ in the presence of ³O₂, HO₂ radical, and NO, leading to the formation of HOOH₂CS(O)₂C(O)H, [•]OH, SO₂, HC(O)OH, H₂C(O), CO₂, CH₃OH, O₂ and CH₂=SO₂. These final products which are formed under tropospheric conditions are indicated in blue.

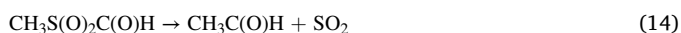
HOOC₂S(O)₂C*OOH. This radical product then undergoes elimination of OH radical to form HOOC₂S(O)₂C(O)H as the final product. In addition, RO₂ radicals may also react with NO and HO₂ radicals in urban atmospheres, indoor air and remote areas, where significant concentrations of NO and HO₂ radicals are present.

The $\text{RO}_2 + \text{NO}$ and $\text{RO}_2 + \text{HO}_2$ mechanisms are illustrated with violet and orange colors, respectively. Initially, RO_2 radical reacts with NO , leading to the production of $\text{CH}_3\text{S}(\text{O})_2\text{CH}_2\text{O}^\bullet$ (see eqn. 11). The transformation of this radical proceeds by two different paths: one involves H-atom abstraction by O_2 to form the products $\text{HO}_2 + \text{CH}_3\text{S}(\text{O})_2\text{C}(\text{O})\text{H}$,

the latter of which then reacts with OH radical. Two H-abstraction paths are available for the reaction of $\text{CH}_3\text{S}(\text{O})_2\text{C}(\text{O})\text{H}$ + OH radical (see eqs (12) and (13))

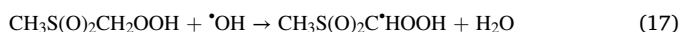
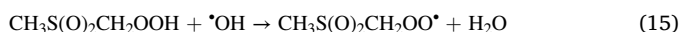


The energy barriers for the H-atom abstraction by OH radical from the methyl group (eq (12)) and the aldehydic group (eq (13)) are reported to be 3.7 and $-2.4 \text{ kcal mol}^{-1}$, respectively (Galano et al., 2004). We used the energy barriers for the $\text{CH}_3\text{C}(\text{O})\text{C}(\text{O})\text{H}$ + $\cdot\text{OH}$ reaction (Galano et al., 2004) for comparison. These values suggest that the barrier for hydrogen abstraction from the methyl in $\text{CH}_3\text{S}(\text{O})_2\text{C}(\text{O})\text{H}$ is higher by $\sim 6 \text{ kcal mol}^{-1}$ compared to the value for hydrogen abstraction from the aldehydic group. Therefore, abstraction of an H-atom from the $-\text{C}(\text{O})\text{H}$ of $\text{CH}_3\text{S}(\text{O})_2\text{C}(\text{O})\text{H}$ to produce $\text{CH}_3\text{S}(\text{O})_2\text{C}^*(\text{O})$ + H_2O products (eq (13)) has the lowest barrier and is the major reaction compared to the other possible path. The formed $\text{CH}_3\text{S}(\text{O})_2\text{C}^*(\text{O})$ reacts with atmospheric O_2 to form $\text{CH}_3\text{S}(\text{O})_2\text{C}(\text{O})\text{OO}^*$ which then further undergoes a 1,5-hydrogen shift followed by C-S single bond scission to form the products sulfene ($\text{CH}_2=\text{S}(\text{O})_2$) + $\cdot\text{C}(\text{O})\text{OOH}$. The $\cdot\text{C}(\text{O})\text{OOH}$ product undergoes carbon dioxide (CO_2) extrusion with release of OH radical through O-O single bond scission. The oxidation of $\text{CH}_3\text{S}(\text{O})_2\text{C}(\text{O})\text{H}$ also proceeds via intramolecular transfer of the methyl group to the C-atom of $-\text{C}(\text{O})\text{H}$, followed by S-C single bond fission leading to the formation of SO_2 + acetaldehyde ($\text{CH}_3\text{C}(\text{O})\text{H}$) (see eqn (14)).

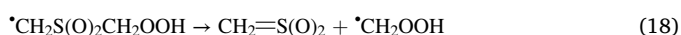


The energy calculations performed in the present work at the M06-2X/aug-cc-pV(T+d)Z level indicate that the barrier height for this reaction (eqn (14)) is $\sim 50.0 \text{ kcal mol}^{-1}$. This suggests that the formation of SO_2 + $\text{CH}_3\text{C}(\text{O})\text{H}$ is not energetically feasible under atmospheric conditions. The second path involves C-S bond rupture of the $\text{CH}_3\text{S}(\text{O})_2\text{CH}_2\text{O}$ radical resulting in formation of $\text{CH}_3\text{S}^*(\text{O})_2$ + formaldehyde (CH_2O).

Similarly, RO_2 reacts with HO_2 radical via the reaction shown in eqn. 10 to form the corresponding hydroperoxide ($\text{CH}_3\text{S}(\text{O})_2\text{CH}_2\text{OOH}$). The fate of this molecule is initiated with H-atom abstraction by OH radical through the reaction paths shown in eqn (15), (16) and (17).



The rate coefficients for the H-atom abstraction from the peroxide (eqn. (15)), methyl (eqn. (16)) and methylene groups (eqn. (17)) are expected to be $\sim 1.0\text{--}2.0 \times 10^{-14} \text{ cm}^3 \text{ molecule}^{-1} \text{ s}^{-1}$ at 298 K (Berasategui et al., 2020b). This value of rate coefficient was adapted from the theoretically calculated rate coefficient reported for the reaction of $\text{CH}_3\text{C}(\text{O})\text{OOH}$ with OH radical at 298 K for comparison (Berasategui et al., 2020b). These results indicate that the reactions shown in eqn. (15), (16) and (17) proceed at almost the same rate. Equation (15) represents a reproduction of the RO_2 radical (i.e., $\text{CH}_3\text{S}(\text{O})_2\text{CH}_2\text{OO}^*$) through the reaction of $\text{CH}_3\text{S}(\text{O})_2\text{CH}_2\text{OOH}$ with $\cdot\text{OH}$. The $\cdot\text{CH}_2\text{S}(\text{O})_2\text{CH}_2\text{OOH}$ formed (see eqn. (16)) undergoes C-S single bond scission leading to $\text{CH}_2=\text{S}(\text{O})_2$ (i.e., sulfene) + $\cdot\text{CH}_2\text{OOH}$ as products (presented in eqn. (18)). Further, the $\cdot\text{CH}_2\text{OOH}$ product formed in this reaction undergoes O-O bond cleavage leading to the formation of $\cdot\text{OH}$ + $\text{H}_2\text{C}(\text{O})$ via eqn. (19) (Berasategui et al., 2020b).



The $\text{CH}_3\text{S}(\text{O})_2\text{C}^*\text{HOH}$ formed (see eqn. (17)) undergoes an OH-shift to the radical center on the C-atom to form the product $\text{CH}_3\text{S}(\text{O})_2\text{CH}(\text{OH})\text{O}^*$, which then further undergoes C-S single bond scission to produce the products $\text{HC}(\text{O})\text{OH}$ + $\text{CH}_3\text{S}^*(\text{O})_2$ (Berasategui et al., 2020a). The fate of $\text{CH}_3\text{S}^*(\text{O})_2$ is reported to be the formation of SO_2 and methyl radical through C-S bond fission (Chen et al., 2021). The formed methyl radical reacts further with $^3\text{O}_2$ to produce CH_3OO radical. The fate of this radical is reported to occur through self-reaction to form CH_3OH + $\text{H}_2\text{C}(\text{O})$ + O_2 (Atkinson et al., 2006). Subsequent reactions of CH_3OO radical with HO_2 and OH radical lead to $\text{HC}(\text{O})\text{OH}$ as the final product (Atkinson et al., 2006). Overall, $\text{DMS}(\text{O})_2$ released into the atmosphere can react with $\cdot\text{OH}$, $\cdot\text{Cl}$, and NO_3^* , and in the presence of O_2 , NO, and HO_2 radicals, serves as a precursor for the formation of $\text{HOCH}_2\text{CS}(\text{O})_2\text{C}(\text{O})\text{H}$, OH radical, CO_2 , O_2 , $\text{CH}_2=\text{SO}_2$, $\text{H}_2\text{C}(\text{O})$, $\text{HC}(\text{O})\text{OH}$, SO_2 , and CH_3OH as final products.

5. Conclusions

Using extensive computational calculations and chemical kinetic modeling, we investigated the energies and kinetics of the atmospheric oxidation of $\text{DMS}(\text{O})_2$ with $\cdot\text{OH}$, $\cdot\text{Cl}$ and NO_3^* , as well as the fate of the C-centered $\text{DMS}(\text{O})_2$ product radical that is formed in all three cases, when it is intercepted by $^3\text{O}_2$. Our main findings in this work are summarized as follows:

- The energetics and kinetics calculations show that the channel involving abstraction of an H-atom from CH_3 by $\cdot\text{OH}$, $\cdot\text{Cl}$, or NO_3^* (in contrast to addition to the sulfur of $\text{DMS}(\text{O})_2$), leading to the formation of $\text{CH}_3\text{S}(\text{O})_2\text{C}^*\text{H}_2$, is the dominant path.
- Under atmospheric conditions where the concentrations of NO and HO_2 radical are low, the formed $\text{CH}_3\text{S}(\text{O})_2\text{C}^*\text{H}_2$ radical reacts with O_2 to form RO_2 radical, which then proceeds via an auto-oxidation mechanism to form $\text{HOCH}_2\text{CS}(\text{O})_2\text{CHO}$ + OH radical as products.
- Under rich NO and HO_2 conditions, such as occurs in urban areas, the formed $\text{CH}_3\text{S}(\text{O})_2\text{C}^*\text{H}_2$ can further react with O_2 , followed by subsequent reactions with NO or HO_2 to form CH_2O + CH_3OH + $\text{HC}(\text{O})\text{OH}$ + SO_2 + O_2 + CO_2 + $\text{CH}_2=\text{SO}_2$ as final products.
- The cumulative atmospheric lifetime of $\text{DMS}(\text{O})_2$ with respect to its interactions with $\cdot\text{OH}$, $\cdot\text{Cl}$, and NO_3^* is estimated to be 3–5 days, indicating that this compound is short-lived in the atmosphere.
- The final reaction products generated in NO- and HO_2 - rich areas may have significant effects on air quality and climate change in the Earth's atmosphere.

CRedit authorship contribution statement

Parandaman Arathala: performed the electronic structure calculations, carried out the MESMER kinetics calculations, wrote the initial draft of the manuscript, and helped with the edits for the review process. **Rabi A. Musah:** conceived the project, acquired funding support, supervised its implementation, and edited the manuscript before and after the review process.

Declaration of competing interest

The authors declare that they have no known competing financial interests or personal relationships that could have appeared to influence the work reported in this paper.

Data availability

Supporting Information in the separate file

Acknowledgements

The financial support of the National Science Foundation (grant numbers 1310350 and 1710221) to R.A.M is gratefully acknowledged. The authors are also grateful for the support of the High-Performance Computing Center at the University at Albany-SUNY, as well as the Research Foundation of SUNY.

Appendix A. Supplementary data

Supplementary data to this article can be found online at <https://doi.org/10.1016/j.atmosenv.2023.119990>.

References

- Anglada, J.M., Solé, A., 2017. The atmospheric oxidation of HONO by OH, Cl, and ClO radicals. *J. Phys. Chem. A* 121, 9698–9707.
- Arathala, P., Musah, R.A., 2019. Theoretical studies of the gas-phase reactions of S-methyl methanesulfinothioate (dimethyl thiosulfinate) with OH and Cl radicals: reaction mechanisms, energetics, and kinetics. *J. Phys. Chem. A* 123, 8448–8459.
- Arathala, P., Musah, R.A., 2021. Oxidation of dipropyl thiosulfinate initiated by Cl radicals in the gas phase: implications for atmospheric chemistry. *ACS Earth Space Chem* 5, 2878–2890.
- Arathala, P., Musah, R.A., 2022. Theoretical study of the atmospheric chemistry of methane sulfonamide initiated by OH radicals and the $\text{CH}_3\text{S}(\text{O})_2\text{NH} + {}^3\text{O}_2$ reaction. *J. Phys. Chem. A* 126, 9447–9460.
- Arathala, P., Musah, R.A., 2023. Quantum chemical and kinetic study of the gas-phase reactions of methane sulfonamide with Cl atom and the fate of ${}^1\text{CH}_2\text{S}(\text{=O})_2\text{NH}_2$ with ${}^3\text{O}_2$ in the atmosphere. *ACS Earth Space Chem* 7, 1049–1059.
- Arsene, C., Barnes, I., Becker, K.H., Mocanu, R., 2001. FT-IR product study on the photo-oxidation of dimethyl sulphide in the presence of NO_x —temperature dependence. *Atmos. Environ.* 35, 3769–3780.
- Asatryan, R., Bozzelli, J.W., 2008. Formation of a criegee intermediate in the low-temperature oxidation of dimethyl sulfoxide. *Phys. Chem. Chem. Phys.* 10, 1769–1780.
- Atkinson, R., 2000. Atmospheric chemistry of VOCs and NO_x . *Atmos. Environ.* 34, 2063–2101.
- Atkinson, R., Arey, J., 2003. Atmospheric degradation of volatile organic compounds. *Chem. Rev.* 103, 4605–4638.
- Atkinson, R., Baulch, D.L., Cox Jr., R.A., Hampson, R.F., Kerr, J.A., Troe, J., 1989. Evaluated kinetic and photochemical data for atmospheric chemistry: supplement III. IUPAC subcommittee on gas kinetic data evaluation for atmospheric chemistry. *J. Phys. Chem. Ref. Data* 18, 881–1097.
- Atkinson, R., Baulch, D.L., Cox, R.A., Crowley, J.N., Hampson, R.F., Hynes, R.G., Jenkin, M.E., Rossi, M.J., Troe, J., Subcommittee, I., 2006. Evaluated kinetic and photochemical data for atmospheric chemistry: volume II – gas phase reactions of organic species. *Atmos. Chem. Phys.* 6, 3625–4055.
- Ayers, G.P., Gillett, R.W., 2000. DMS and its oxidation products in the remote marine atmosphere: implications for climate and atmospheric chemistry. *J. Sea Res.* 43, 275–286.
- Ball, P., 2000. Fast-acting atmospheric detergent. *Nature*. <https://doi.org/10.1038/news001109-1>.
- Barnes, I., Hjorth, J., Mihalopoulos, N., 2006. Dimethyl sulfide and dimethyl sulfoxide and their oxidation in the atmosphere. *Chem. Rev.* 106, 940–975.
- Bentley, R., Chasteen, T.G., 2004. Environmental VOCs—formation and degradation of dimethyl sulfide, methanethiol and related materials. *Chemosphere* 55, 291–317.
- Berasategui, M., Amedro, D., Edtbauer, A., Williams, J., Lelieveld, J., Crowley, J.N., 2020a. Kinetic and mechanistic study of the reaction between methane sulfonamide ($\text{CH}_3\text{S}(\text{O})_2\text{NH}_2$) and OH. *Atmos. Chem. Phys.* 20, 2695–2707.
- Berasategui, M., Amedro, D., Vereecken, L., Lelieveld, J., Crowley, J.N., 2020b. Reaction between $\text{CH}_3\text{C}(\text{O})\text{OOH}$ (peracetic acid) and OH in the gas phase: a combined experimental and theoretical study of the kinetics and mechanism. *Atmos. Chem. Phys.* 20, 13541–13555.
- Berresheim, H., Tanner, D., Eisele, F., 1993. Method for real-time detection of dimethyl sulfone in ambient air. *Anal. Chem.* 65, 3168–3170.
- Boyd, A.A., Flaud, P.-M., Daugey, N., Lesclaux, R., 2003. Rate constants for $\text{RO}_2 + \text{HO}_2$ reactions measured under a large excess of HO_2 . *J. Phys. Chem. A* 107, 818–821.
- Brimblecombe, P., 2013. *The Global Sulfur Cycle, Treatise on Geochemistry*, second ed. Elsevier Inc., pp. 559–591.
- Bunkan, A.J.C., Hetzler, J., Mikoviny, T., Wisthaler, A., Nielsen, C.J., Olzmann, M., 2015. The reactions of N-methylformamide and N,N-dimethylformamide with OH and their photo-oxidation under atmospheric conditions: experimental and theoretical studies. *Phys. Chem. Chem. Phys.* 17, 7046–7059.
- Chen, Q., Sherwen, T., Evans, M., Alexander, B., 2018. DMS oxidation and sulfur aerosol formation in the marine troposphere: a focus on reactive halogen and multiphase chemistry. *Atmos. Chem. Phys.* 18, 13617–13637.
- Chen, J., Berndt, T., Möller, K.H., Lane, J.R., Kjaergaard, H.G., 2021. Atmospheric fate of the CH_3SOO radical from the $\text{CH}_3\text{S} + \text{O}_2$ equilibrium. *J. Phys. Chem. A* 125, 8933–8941.
- Cox, R.A., Hewitt, C.N., Liss, P.S., Lovelock, K.R., Shine, J.E., Thrush, B.A., Ravishankara, A.R., Rudich, Y., Talukdar, R., Barone, S.B., 1997. Oxidation of atmospheric reduced sulphur compounds: perspective from laboratory studies. *Philos. Trans. R. Soc. B* 352, 171–182.
- Davis, D., Chen, G., Kasibhatla, P., Jefferson, A., Tanner, D., Eisele, F., Lenschow, D., Neff, W., Berresheim, H., 1998. DMS oxidation in the antarctic marine boundary layer: comparison of model simulations and held observations of DMS, DMSO , DMSO_2 , $\text{H}_2\text{SO}_4(\text{g})$, $\text{MSA}(\text{g})$, and $\text{MSA}(\text{p})$. *J. Geophys. Res.* 103, 1657–1678.
- Draper, D.C., Farmer, D.K., Desyaterik, Y., Fry, J.L., 2015. A qualitative comparison of secondary organic aerosol yields and composition from ozonolysis of monoterpenes at varying concentrations of NO_2 . *Atmos. Chem. Phys.* 15, 12267–12281.
- Edtbauer, A., Stöner, C., Pfannerstill, E.Y., Berasategui, M., Walter, D., Crowley, J.N., Lelieveld, J., Williams, J., 2020. A new marine biogenic emission: methane sulfonamide (MSAM), dimethyl sulfide (DMS), and dimethyl sulfone (DMSO_2) measured in air over the Arabian Sea. *Atmos. Chem. Phys.* 20, 6081–6094.
- Falbe-Hansen, H., Sørensen, S., Jensen, N.R., Pedersen, T., Hjorth, J., 2000. Atmospheric gas-phase reactions of dimethylsulphoxide and dimethylsulphone with OH and NO_3 radicals, Cl atoms and ozone. *Atmos. Environ.* 34, 1543–1551.
- Frisch, M.J., Trucks, G.W., Schlegel, H.B., Scuseria, G.E., Robb, M.A., Cheeseman, J.R., Scalmani, G., Barone, V., Petersson, G.A., Nakatsuji, H., al, e., 2016. Gaussian 16. Gaussian, Inc., Wallingford, CT.
- Fu, Z., Xie, H.-B., Elm, J., Liu, Y., Fu, Z., Chen, J., 2022. Atmospheric autoxidation of organophosphate esters. *Environ. Sci. Technol.* 56, 6944–6955.
- Fukui, K., 1981. The path of chemical reactions - the IRC approach. *Acc. Chem. Res.* 14, 363–368.
- Galano, A., Alvarez-Idaboy, J.R., Ruiz-Santoyo, M.E., Vivier-Bunge, A., 2004. Mechanism and kinetics of the reaction of OH radicals with glyoxal and methylglyoxal: a quantum Chemistry+CVT/SCT approach. *ChemPhysChem* 5, 1379–1388.
- Glowacki, D.R., Liang, C.-H., Morley, C., Pilling, M.J., Robertson, S.H., 2012. MESMER: an open-source master equation solver for multi-energy well reactions. *J. Phys. Chem. A* 116, 9545–9560.
- Harvey, G.R., Lang, R.F., 1986. Dimethylsulfoxide and dimethylsulfone in the marine atmosphere. *Geophys. Res. Lett.* 13, 49–51.
- Hofzumahaus, A., Rohrer, F., Lu, K., Bohn, B., Brauers, T., Chang, C.-C., Fuchs, H., Holland, F., Kita, K., Kondo, Y., Li, X., Lou, S., Shao, M., Zeng, L., Wahner, A., Zhang, Y., 2009. Amplified trace gas removal in the troposphere. *Science* 324, 1702–1704.
- Hyttinen, N., Knap, H.C., Rissanen, M.P., Jørgensen, S., Kjaergaard, H.G., Kurtén, T., 2016. Unimolecular HO_2 loss from peroxy radicals formed in autoxidation is unlikely under atmospheric conditions. *J. Phys. Chem. A* 120, 3588–3595.
- Jasper, A.W., Miller, J.A., 2014. Lennard-Jones parameters for combustion and chemical kinetics modeling from full-dimensional intermolecular potentials. *Combust. Flame* 161, 101–110.
- Jensen, N.R., Hjorth, J., Lohse, C., Skov, H., Restelli, G., 1991. Products and mechanism of the reaction between NO_3 and dimethylsulphide in air. *Atmos. Environ., Part A* 25, 1897–1904.
- Khan, M.A.H., Ashfold, M.J., Nickless, G., Martin, D., Watson, L.A., Hamer, P.D., Wayne, R.P., Canosa-Mas, C.E., Shallcross, D.E., 2008. Night-time NO_3 and OH radical concentrations in the United Kingdom inferred from hydrocarbon measurements. *Atmos. Sci. Lett.* 9, 140–146.
- Khan, M.A.H., Gillespie, S.M.P., Razis, B., Xiao, P., Davies-Coleman, M.T., Percival, C.J., Derwent, R.G., Dyke, J.M., Ghosh, M.V., Lee, E.P.F., Shallcross, D.E., 2016. A modelling study of the atmospheric chemistry of DMS using the global model, STOCHEM-CRI. *Atmos. Environ.* 127, 69–79.
- Kumar, A., Rajakumar, B., 2019. Cl atom initiated photo-oxidation of mono-chlorinated propanes to form carbonyl compounds: a kinetic and mechanistic approach. *J. Phys. Chem. A* 123, 723–741.
- Kurtén, T., Lane, J.R., Jørgensen, S., Kjaergaard, H.G., 2011. A computational study of the oxidation of SO_2 to SO_3 by gas-phase organic oxidants. *J. Phys. Chem. A* 115, 8669–8681.
- Kurylo, M.J., Orkin, V.L., 2003. Determination of atmospheric lifetimes via the measurement of OH radical kinetics. *Chem. Rev.* 103, 5049–5076.
- Lee, B.H., Mohr, C., Lopez-Hilfiker, F.D., Lutz, A., Hallquist, M., Lee, L., Romer, P., Cohen, R.C., Iyer, S., Kurtén, T., et al., 2016. Highly functionalized organic nitrates in the southeast United States: contribution to secondary organic aerosol and reactive nitrogen budgets. *Proc. Natl. Acad. Sci. U.S.A.* 113, 1516–1521.
- Lelieveld, J., Butler, T.M., Crowley, J.N., Dillon, T.J., Fischer, H., Ganzeveld, L., Harder, H., Lawrence, M.G., Martinez, M., Taraborrelli, D., Williams, J., 2008. Atmospheric oxidation capacity sustained by a tropical forest. *Nature* 452, 737–740.
- Lily, M., Baidya, B., Wang, W., Liu, F., Chandra, A.K., 2020. Atmospheric chemistry of $\text{CHF}_2\text{CF}_2\text{OCH}_2\text{CF}_3$: reactions with Cl atoms, fate of $\text{CHF}_2\text{CF}_2\text{OCH}_2\text{CF}_3$ radical, formation of OH radical and criegee intermediate. *Atmos. Environ.* 242, 117805.
- Logan, J.A., 1985. Tropospheric ozone: seasonal behavior, trends, and anthropogenic influence. *J. Geophys. Res.* 90, 10463–10482.
- Ma, F., Ding, Z., Elm, J., Xie, H.-B., Yu, Q., Liu, C., Li, C., Fu, Z., Zhang, L., Chen, J., 2018. Atmospheric oxidation of piperazine initiated by -Cl: unexpected high nitrosamine yield. *Environ. Sci. Technol.* 52, 9801–9809.
- Maguta, M.M., Stenstrom, Y., Nielsen, C.J., 2016. Kinetic and theoretical study of the nitrate (NO_3) radical gas phase reactions with N-nitrosodimethylamine and N-nitrosodiethylamine. *J. Phys. Chem. A* 120, 6970–6977.
- Mardyukov, A., Schreiner, P.R., 2018. Atmospherically relevant radicals derived from the oxidation of dimethyl sulfide. *Acc. Chem. Res.* 51, 475–483.

- Miller, W.H., 1979. Tunneling corrections to unimolecular rate constants, with application to formaldehyde. *J. Am. Chem. Soc.* 101, 6810–6814.
- Mishra, B.K., Lily, M., Deka, R.C., Chandra, A.K., 2016. A theoretical insight into atmospheric chemistry of HFE-7100 and perfluoro-butyl formate: reactions with OH radicals and Cl atoms and the fate of alkoxy radicals. *New J. Chem.* 40, 6148–6155.
- Newland, M.J., Bryant, D.J., Dunmore, R.E., Bannan, T.J., Acton, W.J.F., Langford, B., Hopkins, J.R., Squires, F.A., Dixon, W., Drysdale, W.S., et al., 2021. Low-NO atmospheric oxidation pathways in a polluted megacity. *Atmos. Chem. Phys.* 21, 1613–1625.
- Nicovich, J.M., Mazumder, S., Laine, P.L., Wine, P.H., Tang, Y., Bunkan, A.J.C., Nielsen, C.J., 2015. An experimental and theoretical study of the gas phase kinetics of atomic chlorine reactions with CH_3NH_2 , $(\text{CH}_3)_2\text{NH}$, and $(\text{CH}_3)_3\text{N}$. *Phys. Chem. Chem. Phys.* 17, 911–917.
- Noga, J., Bartlett, R.J., 1987. The full CCSDT model for molecular electronic structure. *J. Chem. Phys.* 86, 7041–7050.
- Nøjgaard, J.K., 2010. Indoor measurements of the sum of the nitrate radical, NO_3 , and nitrogen pentoxide, N_2O_5 in Denmark. *Chemosphere* 79, 898–904.
- Orlando, J.J., Tyndall, G.S., 2012. Laboratory studies of organic peroxy radical chemistry: an overview with emphasis on recent issues of atmospheric significance. *Chem. Soc. Rev.* 41, 6294–6317.
- Pagonis, D., Price, D.J., Algrim, L.B., Day, D.A., Handschy, A.V., Stark, H., Miller, S.L., de Gouw, J., Jimenez, J.L., Ziemann, P.J., 2019. Time-resolved measurements of indoor chemical emissions, deposition, and reactions in a university art museum. *Environ. Sci. Technol.* 53, 4794–4802.
- Parandaman, A., Kumar, M., Francisco, J.S., Sinha, A., 2018. Organic acid formation from the atmospheric oxidation of gem diols: reaction mechanism, energetics, and rates. *J. Phys. Chem. A* 122, 6266–6276.
- Piletic, I.R., Edney, E.O., Bartolotti, L.J., 2017. Barrierless reactions with loose transition states govern the yields and lifetimes of organic nitrates derived from isoprene. *J. Phys. Chem. A* 121, 8306–8321.
- Rao, P.K., Deka, R.C., Gour, N.K., Gejji, S.P., 2018. Understanding the atmospheric oxidation of HFE-7500 ($\text{C}_3\text{F}_7\text{CF}(\text{OC}_2\text{H}_5)\text{CF}(\text{CF}_3)_2$) initiated by Cl atom and NO_3 radical from theory. *J. Phys. Chem. A* 122, 6799–6808.
- Riedel, K., Lassey, K., 2008. Detergent of the atmosphere water. *Atmosphere* 16, 22–23.
- Rollins, A.W., Browne, E.C., Min, K.-E., Pusede, S.E., Wooldridge, P.J., Gentner, D.R., Goldstein, A.H., Liu, S., Day, D.A., Russell, L.M., Cohen, R.C., 2012. Evidence for NO_x control over nighttime SOA formation. *Science* 337, 1210–1212.
- Sievert, S.M., Kiene, R.P., Schulz-Vogt, H.N., 2007. The sulfur cycle. *Oceanography* 20, 117–123.
- Spicer, C.W., Chapman, E.G., Finlayson-Pitts, B.J., Plastringe, R.A., Hubbe, J.M., Fast, J.D., Berkowitz, C.M., 1998. Unexpectedly high concentrations of molecular chlorine in coastal air. *Nature* 394, 353–356.
- Dunning Jr., T.H., Peterson, K.A., Wilson, A.K., 2001. Gaussian basis sets for use in correlated molecular calculations. X. The atoms aluminum through argon revisited. *J. Chem. Phys.* 114, 9244–9253.
- Tyndall, G.S., Ravishankara, A.R., 1991. Atmospheric oxidation of reduced sulfur species. *Int. J. Chem. Kinet.* 23, 483–527.
- Wang, W., Ezell, M.J., Ezell, A.A., Soskin, G., Finlayson-Pitts, B.J., 2002. Rate constants for the reactions of chlorine atoms with a series of unsaturated aldehydes and ketones at 298 K: structure and reactivity. *Phys. Chem. Chem. Phys.* 4, 1824–1831.
- Watts, S.F., Brimblecombe, P., Watson, A.J., 1990. Methanesulphonic acid, dimethyl sulphoxide and dimethyl sulphone in aerosols. *Atmos. Environ., Part A* 24, 353–359.
- Webb, A.L., van Leeuwe, M.A., den Os, D., Meredith, M.P., Venables, H.J., Stefels, J., 2019. Extreme spikes in DMS flux double estimates of biogenic sulfur export from the antarctic coastal zone to the atmosphere. *Sci. Rep.* 9, 2233.
- Wilson, A.K., Dunning, T.H., 2004. The HSO–SOH isomers revisited: the effect of tight d functions. *J. Phys. Chem. A* 108, 3129–3133.
- Wingenter, O.W., Sive, B.C., Blake, N.J., Blake, D.R., Rowland, F.S., 2005. Atomic chlorine concentrations derived from ethane and hydroxyl measurements over the equatorial pacific ocean: implication for dimethyl sulfide and bromine monoxide. *J. Geophys. Res. Atmos.* 110 (D20).
- Xie, H.-B., Ma, F., Wang, Y., He, N., Yu, Q., Chen, J., 2015. Quantum chemical study on Cl-initiated atmospheric degradation of monoethanolamine. *Environ. Sci. Technol.* 49, 13246–13255.
- Yin, F., Grosjean, D., Seinfeld, J.H., 1990. Photooxidation of dimethyl sulfide and dimethyl disulfide. I: mechanism development. *J. Atmos. Chem.* 11, 309–364.
- Zavala-Oseguera, C., Alvarez-Idaboy, J.R., Merino, G., Galano, A., 2009. OH radical gas phase reactions with aliphatic ethers: a variational transition state theory study. *J. Phys. Chem. A* 113, 13913–13920.
- Zhao, Y., Truhlar, D.G., 2008. The M06 suite of density functionals for main group thermochemistry, thermochemical kinetics, noncovalent interactions, excited states, and transition elements: two new functionals and systematic testing of four M06-class functionals and 12 other functionals. *Theor. Chem. Acc.* 120, 215–241.